A probabilistic model for predicting the uncertainties of the humid stiction phenomenon on hard materials

T.V. Hoang[a,1], L. Wu[a], S. Paquay[b], A. C. Obreja[c], R. Voicu[c], R. Müller[c], J.-C. Golinval[a], L. Noels[a,*]

[a] *University of Liège - Department of Aerospace and Mechanical Engineering, Chemin des Chevreuils 1, B-4000 Liège, Belgium.*
[b] *Open Engineering SA, Rue des Chasseurs-Ardennais 3, B-4031, Liège (Angleur), Belgium.*
[c] *National Institute for R & D in Microtechnologies - IMT Bucharest, 126A, Erou Iancu Nicolae street, 077190, Bucharest, Romania.*

Abstract

Stiction is a major failure in microelectromechanical system (MEMS) devices in which two contacting surfaces can remain stuck together because of the adhesive forces. Due to the difference between the surfaces roughness and the adhesive force range, the real contact areas are usually smaller than the apparent one, resulting in a scatter in the adhesive forces. Consequently, the stiction is an uncertain phenomenon. In this work, we develop a probabilistic model to predict the uncertainties of stiction due to the capillary forces acting on stiff materials. This model contains two levels: at the deterministic level, the model can predict the pull-out adhesive contact forces for a given surface topology; at the probabilistic level, the model generates independent identically distributed surfaces on which the deterministic solution can be applied to evaluate the uncertainties related to the stiction phenomenon.

Keywords: stiction, capillary force, random field, surface generation, Hertz model, DMT model, GW approach

1. Introduction

Because of their intrinsic advantages, e.g. miniature sizes, low power requirement, and reduced manufacturing cost, many micro-electro-mechanical system (MEMS) devices, such as the accelerometers, digital mirrors, pressure sensors, gyroscopes, and resonators, have been innovated and successfully applied in the industry. In spite of their advantages, due to the inherent characteristic of MEMS, such as the large surface area to volume ratio, the relative smoothness of surfaces, the small interfacial gap, and the small restoring forces of the compliant structures, the contact between their components can lead to the permanent adhesion of their moving parts. This physical phenomenon, named "stiction", is a common failure of MEMS devices [1].

The stiction is the combination of stick and friction which is due to the adhesive forces such as van der Waals (vdW) forces, capillary forces ... In humid conditions, due to the presence of condensing water between the two contacting surfaces, the capillary forces resulting from the negative relative pressure inside the condensing water layers can lead to the stiction of these surfaces. This phenomenon is named "humid stiction". The condensing water layers, the root of humid stiction, strongly depend on the surfaces topologies on which they are formed [1]. However, the topology of rough MEMS surfaces is characterized by a degree of randomness at the nano-scale, making the humid stiction an uncertain phenomenon. This uncertainty was

*Corresponding author, Phone: +32 4 366 48 26, Fax: +32 4 366 95 05
Email address: L.Noels@ulg.ac.be (L. Noels)
[1] PhD candidate at the Belgian National Fund for Education at the Research in Industry and Farming.

experimentally observed: in [1], at a 70%-humidity level, the difference between the highest and the lowest adhesive energies –the energies to completely separate the contacting surfaces– was found to be about 200%; in [2], at a 85%-humidity level, this difference was about 300%. Therefore, probabilistic numerical contact models are required in order to make the humid stiction failure predictable and avoidable. To fulfill these requirements, these models should have two features: (i) at the deterministic level, for a well-defined contact surface topology, the numerical model should be able to predict the contact forces; (ii) at the uncertainty quantification level, the numerical contact model should be able to quantify the uncertainties on the contact forces and on the risk of stiction.

For this first feature, the numerical contact theories have a long history. Based on the Hertz non-adhesive elastic contact theory for spherical asperities [3], three common asperity contact theories were developed for the adhesive case, (i) the Johnson-Kendall-Robert (JKR) theory [4], (ii) the Derjaguin-Muller-Toporov (DMT) theory [5], and (iii) the Maugis theory [6, 7]. The JKR theory assumes that the adhesive forces are applied solely inside the contact area. This theory can thus be applied for soft materials, and short-range adhesive forces, such as vdW forces. In contrast, the DMT theory assumes that the adhesive contact forces are applied outside the contact area, consequently it is applicable for hard materials and long-range adhesive forces, such as capillary forces. The third theory, the Maugis one, is a transition solution between these two models. For the humid stiction case of interest, both the Maugis and DMT theories are applicable. Besides those asperity models, the adhesive contact, due to vdW forces, between asperities has also been studying using molecular dynamics (MD) methods [8]. MD methods were also used to study the adhesive interactions due to vdW forces of silicon [9], silica [10], and silicon carbide [11] nano-particles. These studies have shown that the JKR and DMT models are valid up to given contact interference distances. Finally, the adhesive interaction between a flat surface and a sphere has been modeled using the finite element method [12] by representing the vdW forces through a Lennard-Jones potential. This model was compared to MD simulations.

To evaluate the contact forces at the surface level from the asperity contact forces, the most common method is the statistical approach [13, 14, 15]. This so-called "Greenwood-Williamson" (GW) method was considered in several stiction models [1, 16, 17], including for structural finite element analyzes [18]. In this approach, two important assumptions are made: (i) the asperities are represented at their local maximum by their curvature; (ii) the interactions between the contacting asperities of a surface are neglected. By considering the surface as a second order stationary Gaussian random field, the distribution of maxima can be obtained from the statistical parameters of this field. Using the previous two assumptions, the contact forces can be evaluated at the surface level by integrating the asperity contact forces weighted by the statistical distribution of maxima.

However, there are some cautions to be exercised when applying this statistical approach. For instance, the validity of the first assumption is questionable in practice as one asperity can include many maxima. This limitation was reported by Greenwood [19], one of the authors of statistical approach. In addition, in the case of humid stiction, the second assumption, *i.e.* neglecting the interaction among the asperities of a surface, has a short validity range since the condensing water layers of different contacting asperities can merge together, especially at high humidity levels. This merging phenomenon, named "saturation", was reported in [1]. Moreover, because of the Gaussian nature of the random field, the surface contact forces obtained with the statistical approach can be seen as the average solution of contact forces from (a infinite number of) different individual surfaces. While the result of the statistical approach is an average solution corresponding to an infinite surface, the experimental results of humid stiction tests on finite surfaces show an important uncertainty [1, 2]. In addition, with the statistical approach, because of the Gaussian nature of the random fields, asperities of much higher height than the ones experimentally observed are considered in the distribution. Although their probability of existence is small, their induced contact forces are much higher and the solution converges to values different from the ones observed experimentally by several orders of magnitude. In [1], to obtain numerical results of the same order of magnitude as the experimental ones, the authors have changed the integral limits of the statistical integration process. However the determination of these limits is delicate. Moreover, in the case of poly-silicon, the considered material in this paper, there is little plasticity and the determination of the limits cannot be physically motivated.

Besides the statistical approach, the finite element method is also a candidate to model the stiction of

rough surfaces [20, 21]. However a finite element model is costly in terms of computation due to the high ratio of the surface size to the height of the condensing water layers, and due to the non-linearity of the adhesive contact problem, which limits its applicability when performing uncertainty quantification.

In this work we propose an alternative to the usual GW asperity contact theory formulation.

At first, we develop a modified DMT model that is applied on a defined surface topology, either obtained experimentally or numerically generated. In this model the Hertz contact repulsive forces and the humid adhesive forces are computed separately as their interaction ranges are different. The Hertz repulsive forces are evaluated locally at each contacting asperity, but the adhesive forces are not. Instead the global water interaction area is evaluated from the geometrical parameters of the deformed asperities, predicted by the Hertz theory, and from the topology of the whole interacting surfaces. The adhesive forces due to the capillary forces can then be calculated from this water interaction area. This method allows capturing the saturation phenomenon naturally. However it does not account for the asperity deformation resulting from the adhesive forces and is thus valid for stiff materials only.

Secondly, to quantify the uncertainties in the contact forces, we could apply the modified DMT approach on several experimentally measured samples. However, this would require a huge number of experimental surfaces due to the important observed uncertainties. To reduce the number of fabricated experimental surfaces, a probabilistic approach is implemented in this work. Considering the surfaces as a stationary Gaussian random field, defined from some limited measurements, this field can be characterized by the correlation function or the power spectrum density (psd) function. Based on the spectral representation theory [22, 23], the surface is simulated by generating independent identically distributed fields from this psd function. By applying the modified DMT approach on each generated surface, a set of surface contact forces can be obtained, from which the uncertainties are in turn evaluated.

The structure of this paper is as follows. In Section 2, after a brief introduction of the physical mechanism of humid stiction, the contact theories of JKR, DMT, and Maugis are summarized. In the end of Section 2, the modified DMT method for the asperity contact problem is introduced. In Section 3, the GW statistical approach and its limitations for humid stiction are reviewed. To avoid these drawbacks, the probabilistic modified DMT approach for rough surface contacts is developed. In this section, the numerical predictions of the GW statistical approach and of the modified DMT approach, obtained from experimental topology measurements of poly-silicon surfaces, are compared. These numerical results illustrate the limitations of the GW statistical approach for humid stiction problems. Section 4 deals with those observed uncertainties. To this end, from a limited number of experimental surfaces, a psd function is estimated and is used to generate independent surfaces. The modified DMT approach can then be applied on each generated surface to evaluate a set on contact forces, from which the uncertainties in the contact forces and on the adhesive energies can be identified. The numerical results in this section show that the uncertainties are important at low humidity levels, and that they depend on the size of the considered surfaces. Finally the pull-out test predictions are compared in Section 5 with adhesive experiments on micro beams reported in the literature [1] to evaluate the numerical models.

2. Asperity contact theories

In this section, the physical mechanism of humid stiction is briefly described in the case of a poly-silicon asperity interacting with a poly-silicon surface. The main equations of the JKR, DMT, and Maugis asperity contact theories are then given. Finally, the modified DMT method for an asperity interacting with a flat plane is introduced.

2.1. Physical mechanism of humid stiction

Capillary forces result from the negative relative pressure inside the water condensing between two contacting bodies in humid environments. They result from two contributions, see Fig. 1(b): (i) The Laplace pressure inside the meniscus [24]; (ii) The disjoint pressure inside the adsorbed surface layer [2, 25, 27].

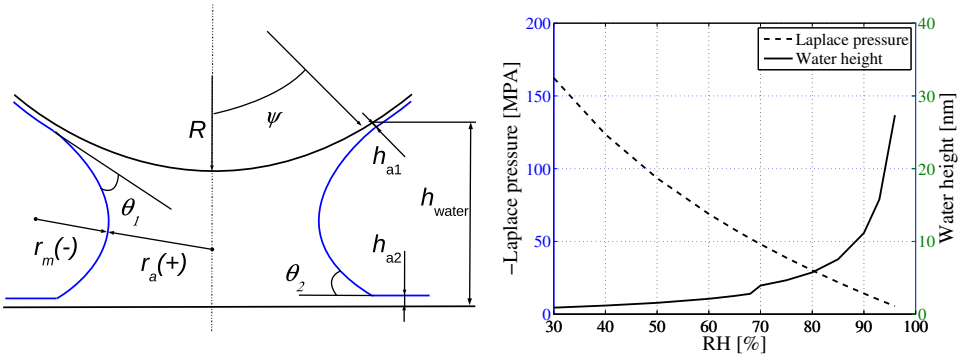

(a) Geometry of condensing water (b) Laplace pressure and water height

Figure 1: The configuration of condensing water. (a) Meniscus and absorbed surface layers condensing between a sphere and a half space (for a negative meridian radius r_m and a positive azimuthal radius r_a). (b)The evolutions of the Laplace pressure and of the water height in terms of the humidity level.

A meniscus is characterized by the contact angles θ_1, θ_2, which depend on the surfaces properties, and by the Kelvin radius r_K, which is defined by

$$r_K = \frac{\gamma_{\rm LG} V_m}{\mathcal{R} T \ln p/p_s}, \tag{1}$$

where $\gamma_{\rm LG}$ is the liquid vapor energy, V_m is the liquid molar volume, $\mathcal{R}$ is the universal gas constant, T is the absolute temperature, p is the actual vapor pressure, and p_s is the saturated vapor pressure. The Laplace pressure inside the meniscus is calculated by

$$\Delta P = \frac{\gamma_{\rm LG}}{r_K} = \frac{\mathcal{R} T \ln RH}{V_m}, \tag{2}$$

where RH is the relative humidity defined by p/p_s. In case of water condensation $V_m = 0.018$ L/mol and $\gamma_{\rm LG} = 0.072$ N/m at $T = 300$ K, and the Kelvin radius is calculated by

$$r_K = \frac{\gamma_{\rm LG} V_m}{\mathcal{R} T \ln p/p_s} = \frac{0.53}{\ln RH} \text{ [nm]} < 0\,. \tag{3}$$

In all generalities, the Kelvin radius is related to the azimuthal radius r_a and to the meridional radius r_m, see Fig. 1(a), following

$$\frac{1}{r_K} = \frac{1}{r_a} + \frac{1}{r_m}\,. \tag{4}$$

If the sphere radius R is much higher (in absolute value) than the Kelvin radius r_K, the azimuthal radius is much larger than the meridional one, so that the Kelvin radius is approximated to the meridional radius: $r_K \simeq r_m < 0$. The height of the meniscus between a sphere and a half space can thus be approximated by

$$h_{\rm men} \simeq -r_K(\cos(\theta_1 + \psi) + \cos\theta_2), \tag{5}$$

where ψ is the subtended angle, see Fig. 1(a). Still considering the case of a sphere radius R much higher (in absolute value) than the Kelvin radius r_K, the subtended angle can be approximated by $\psi \approx \cos^{-1}\frac{R-h_{\rm men}}{R} << 1$ and the meniscus height becomes $h_{men} = -r_K(\cos\theta_1 + \cos\theta_2)$ [26].

The second contribution to the capillary forces is the disjoint pressure inside the adsorbed surface layer. This absorbed surface layer is due to the vdW forces acting between the water molecules and the molecules of the hydrophilic surfaces. In [27], the configuration of the absorbed surface layer was studied experimentally. Below 30 % humidity, the layer behaves as an ice-like network, with a thickness reaching up to three water

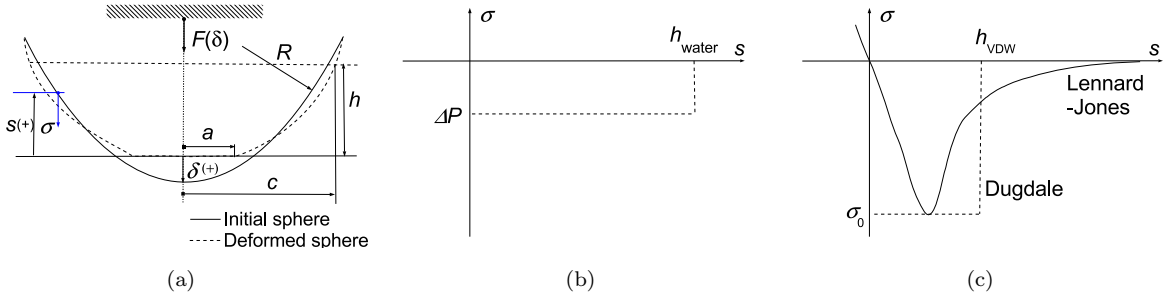

(a) (b) (c)

Figure 2: The asperity adhesive contact problem. (a) The configuration of the adhesive contact between a sphere and a flat surface. Depending on the considered physical problem, the adhesive pressure height h can be either the height of condensing water h_{water} or the range of the vdW adhesive pressure h_{vdW}, the adhesive radius c can be either the water condensing radius c_{water} or the vdW adhesive radius c_{vdW}. (b) Evolution of the adhesive pressure in terms of the contact distance in case of capillary stiction. (c) Evolution of adhesive pressure in terms of the contact distance in case of vdW stiction

molecules. The liquid structure appears between 30 and 60% relative humidity, and above 60% relative humidity a liquid water layer lies on top of the ice-like layer. However, it was also found that the thickness of the adsorbed surface layer depends not only on the humidity level but also on the roughness of the surfaces [2, 25]. In [2], it was assumed that between 30% and 65% relative humidity the absorbed surface layer could have an adhesive effect for surfaces having a low roughness to explain the experimental apparent adhesive energies observed in [1]. The evolution of this absorbed surface layer is currently not built on a theoretical background, see the discussion in [2], so it is seen in this paper as a model parameter through its thickness. The models that will be constructed in the following sections can consider it or not, and its effect will be discussed in Section 5 when comparing the model predictions to experiments. Unless stated otherwise, after investigating the values given in [2, 25, 27], we assume that on the poly-silicon surface the absorbed surface layer contains three water molecules with a thickness of 0.9 nm for humidity levels above 65% and the absorbed surface layer is neglected below this humidity level. The disjoint pressure inside the absorbed surface layer is taken equal to the Laplace pressure inside the meniscus, which can be calculated from Eq. (2).

Taking into account those two contributions, the height of the condensing water between a sphere and a half space with a subtended angle $\psi << 1$ is obtained by

$$h_{\text{water}} = h_{\text{men}} + h_{a1} + h_{a2}, \tag{6}$$

where h_{a1}, h_{a2} are the absorbed layer thickness on the two contacting bodies and where h_{meniscus} is obtained from the meniscus equation (5). The evolutions of the Laplace pressure, Eq. (2), and of the water height, Eq. (6), in terms of the humidity levels are ilustrated in Fig. 1(b).

2.2. Analytical asperity contact theories

In order to evaluate the frictionless elastic interaction forces between two mathematically well-defined bodies, such as between a sphere and a flat surface, there are mainly three well-known analytical adhesive contact models based on the Hertz model [3], the JKR [4], the DMT (Derjaguin-Muller-Toporov) [5], and the Maugis [6] models. These works are based on an important assumption: the radius of the contacting area is much smaller than the size of the contacting asperities. In the following, the four models are briefly described for the spherical adhesive contact problem illustrated in Fig. 2.

2.2.1. JKR model

Johnson, Kendall, and Roberts [4] have introduced their frictionless adhesive contact model, which deals with vdW adhesive forces, by assuming that the adhesive force acts only inside the contact area, see Fig. 2. This assumption is valid in case of soft materials and short-range adhesive forces.

2.2.2. DMT model

The DMT model [5] assumes that the adhesive forces act only outside of the contacting area and that they do not have a significant effect on the deformation of the contacting bodies. This assumption is valid in the case of hard materials and long-range adhesive forces. Using this assumption, the repulsive forces and the adhesive forces can be evaluated separately. The repulsive forces are calculated from Hertz model, and the adhesive forces are obtained by integrating the adhesive pressure on the deformed bodies computed from Hertz solution. The original DMT model for vdW adhesive forces is given in terms of the adhesive energy $\omega_{\mathrm{vdW}} = \gamma_1 + \gamma_2 - \gamma_{12}$ of the vdW forces, with γ_1, γ_2, and γ_{12} the surface energies of the two contacting bodies and of their interaction, respectively. Maugis et al. [7] have proved that this model can also be applied in the capillary adhesive cases by using the adhesive energy obtained frome the capilary forces instead of ω_{vdW}.

2.2.3. Maugis model and Kim extension

The Maugis model [6] was originally applied to the cases of vdW adhesive forces. In this model, the vdW adhesive pressure field is assumed to follow the Dugdale assumption, see Fig. 2(c), in which the vdW adhesive pressure σ_{vdW} is constant between the contact radius a and the vdW adhesive radius c_{vdW}. This adhesive radius c_{vdW} is defined as the separation between the two surfaces h_{vdW} for which the vdW forces vanish, see Fig. 2(a). The adhesive pressure σ_{vdW} is chosen as the highest adhesive pressure of the more realistic Lennard-Jones potential and the height h_{vdW} is calculated from the energy conservation condition $\omega_{\mathrm{vdW}} = \sigma_{\mathrm{vdW}} h_{\mathrm{vdW}}$. Owing to the similarity between the Dugdale assumption and the Laplace pressure field inside the condensing water, Maugis model is also applicable in the capillary adhesive cases [7]. Maugis model is characterized by the transition parameter λ, which is defined by

$$\lambda = \frac{2\sigma_0}{(\pi\omega K^2/R)^{1/3}}, \tag{7}$$

where the two variables $\{\sigma_0, \omega\}$ can either hold for $\{\sigma_{\mathrm{vdW}}, \omega_{\mathrm{vdW}}\}$ or for $\{\sigma_{\mathrm{water}}, \omega_{\mathrm{water}}\}$, depending on the application, and $K = \frac{4}{3}\left[(1-\nu_1^2)/E_1 + (1-\nu_2^2)/E_2\right]^{-1}$ is the reduced elastic modulus with ν_1, ν_2 the Poisson ratios of the sphere and the half space respectively, and with E_1, E_2 their Young's moduli.

Finally Kim et al. [28] have extended Maugis model to the non-contacting case in which the contact radius $a = 0$ and the radius $c > 0$. Details on the implementation of the Maugis model and Kim extension can be found in [16].

2.2.4. Modified DMT

For the capillary adhesive problem, in which the adhesive pressure is constant inside the annulus defined by the contact radius a and the condensing water radius c, both Maugis and DMT models can be considered.

Considering the contact problem between an asperity and a flat surface, the two asperity model candidates, Maugis and DMT models, are applicable when the asperity can be assimilated to a sphere in the contact interfering zone. Considering our problem, the humid adhesive contact on poly-silicon surfaces, since the material is hard and as the Laplace pressure is a long-range adhesive force, the adhesive zone is much bigger than the contacting zone (or repulsive zone) at the equilibrium position, *i.e.* when the resulting adhesive contact force is zero. Mathematically speaking, the condensing water height h_{water} is much larger than the equilibrium interference δ_{eq} and the condensing water radius c_{water} is much higher than the contact radius a, see Fig 2(a). Consequently, the real contact profile cannot be assimilated to be a single sphere at both the contacting and adhesive scales, and both DMT and Maugis methods can be inapplicable. In these cases we can assume that: (i) the deformation of the contacting bodies due to the adhesive force is negligible in comparison with the deformation due to the repulsive force in the contacting zone, as in the DMT theory; (ii) the deformation of the contacting body at the distance h_{water} from the flat surface is negligible.

In this section, using these two assumptions, we derive in a straighforward way the resulting model in the case of a spherical asperity for the sake of comparison. We will generalize the model for more complex asperity profiles in the case of rough surfaces interaction in the next section. Using the first assumption, the adhesive force and the repulsive force can be evaluated separately as in the DMT theory. The contact forces are calculated as $F = F_r + F_a$ where F_r is the repulsive force, which can be obtained from Hertz theory,

and F_a is the adhesive force. The adhesive force is the integration of the Laplace pressure on the annulus between the contacting radius a and the water interaction radius c_{water}, see Fig. 2, and is thus computed as $F_a = \Delta P \pi (c_{\text{water}}^2 - a^2)$. Using the second assumption the radius c depends only on the initial profile:

$$c_{\text{water}} = \sqrt{R^2 - (R - \delta - h_{\text{water}})^2}. \tag{8}$$

Eventually, the total adhesive contact force is evaluated by

$$F = F_r + \Delta P \pi [R^2 - (R - \delta - h_{\text{water}})^2 - a^2], \tag{9}$$

where δ is the interference, see Fig. 2(a). In Eq. (9), the rupulsive force F_r and the contating radius a are evaluated from the Hertz theory as

$$a^3 = \frac{RF_r}{K}, \tag{10}$$

$$\delta = \frac{a^2}{R}. \tag{11}$$

As it can be observed, this new method does not require the deformed profile to be evaluated at the radius c as in the DMT method. Owing to this relaxation, the modified DMT model is more flexible when applied to the rough surface contact problem in comparison to the Maugis and DMT models, as it will be performed in Section 3.3.

2.2.5. Comparison of the analytical methods for spherical asperities

The three candidate models to represent the humid stiction problems, *i.e.* the Maugis, DMT, and modified DMT models, are compared on the contact problem of a spherical poly-silicon asperity at difference humidity levels. Using the experimental data from [1], in which the average radius of poly-silicon asperities was measured to be 260.5 nm, we study the cases of radii of 100 nm and 800 nm to analyse the behavior at the extreme cases. The considered poly-silicon material has a Young's modulus $E = 164$ GPa and a Poisson ratio $\nu = 0.23$ [29]. The results of the contact forces between a sphere and a plat surface made of poly-silicon are illustrated in Fig. 3 for the three methods. The extracted adhesive energies, *i.e.* the work required to separate the asperity from the plane, are reported in Tab. 1.

Table 1: Comparison of the adhesive energies [J] obtained with the three methods.

	RH=30%		RH=50%		RH=70%	
	$R = 100$ nm	$R = 800$ nm	$R = 100$ nm	$R = 800$ nm	$R = 100$ nm	$R = 800$ nm
Maugis	5.11×10^{-17}	4.75×10^{-16}	8.07×10^{-17}	7.25×10^{-16}	3.72×10^{-16}	3.14×10^{-15}
DMT	5.11×10^{-17}	4.95×10^{-16}	8.05×10^{-17}	7.32×10^{-16}	3.68×10^{-16}	3.16×10^{-15}
Modified DMT	5.18×10^{-17}	5.22×10^{-16}	8.08×10^{-17}	7.49×10^{-16}	3.68×10^{-16}	3.18×10^{-15}

It can be seen in Fig. 3 that the difference in the contact curves obtained by the different methods is higher for the larger asperity and at the lower humidity levels. Considering the case of 30% humidity and 800 nm-asperity radius, the difference in the adhesive energies is about 10% between the modified DMT method and the Maugis theory, and about 5% between the modified DMT method and the DMT theory, see Tab. 1. For the other cases, the differences of the adhesive energies are negligible (below 3.3%). At 30% humidity, these differences result from having neglected the deformation due to the adhesive pressure in the two DMT theories. In fact, at 30% humidity level, the ratio of the adhesive pressure to the poly-silicon tensile strength is 7.6%. This ratio decreases at higher humidity levels.

The close values obtained by both the DMT and the modified DMT methods validate the second assumption of the modified DMT method: the deformation of the contacting body at a distance h_{water} from the flat surface can be neglected. From this comparison we can conclude that besides Maugis model, which was proved to be valid to model the problem of humid stiction [7], both DMT and modified DMT models are applicable to our problem.

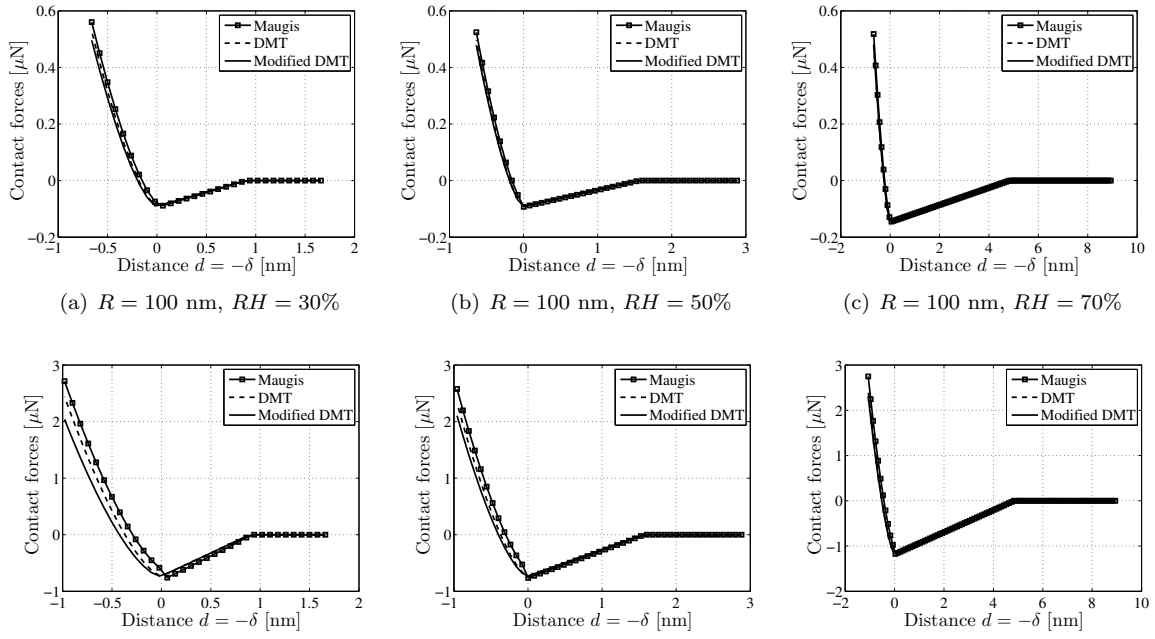

(a) $R = 100$ nm, $RH = 30\%$ (b) $R = 100$ nm, $RH = 50\%$ (c) $R = 100$ nm, $RH = 70\%$

(d) $R = 800$ nm, $RH = 30\%$ (e) $R = 800$ nm, $RH = 50\%$ (f) $R = 800$ nm, $RH = 70\%$

Figure 3: Comparison of the three methods for poly-silicon asperities of radii R=100 nm (upper row) and R=800 nm (lower row) at different humidity levels: 30% (first column), 50% (second column), and 70% (third column).

However, the modified DMT approach is only valid when the asperity deformation due to the adhesive forces can be neglected. In the context of vdW forces at the nano-scale [9], or in the context of softer materials than silicon, this assumption does not hold. One improvement in the modified DMT approach to consider the deformation due to short range forces could be to substitute the Hertz model used to evaluate the repulsive forces by a JKR model, but this requires more investigation.

3. Rough surface contact model

The purpose of this section is to evaluate the contact forces between a rough surface and a flat surface in humid conditions. Some poly-silicon samples were fabricated and measured in order to extract their surface topologies. Two approaches to evaluate the contact forces, the GW statistical approach and a new approach based on the developed modified DMT approach, are presented and compared to each other.

3.1. The experimental poly-silicon surfaces

Using surface micro-machining techniques, see Fig. 4(a), two poly-silicon samples, named S1 and S2, were fabricated at IMT Bucharest. From the $< 100 >$ orientation silicon wafer of p-type, a silicon dioxide layer was grew by thermal technique at 900^oC. On this silicon dioxide layer, a poly-silicon layer was deposited using low pressure chemical vapor deposition (LPCVD) technique. By controlling the temperature, the silane debit, and the deposit time of the LPCVD process, the obtained samples have different topological properties. A scanning electro microscope (SEM) image of sample S1, shown in Fig. 4(b), illustrates the resulting surface topology on which the asperities can clearly be seen.

After manufacturing, the topologies of the two samples were measured by using an atomic force microscopy (AFM) technique at three different locations for each sample. These measurements are named S1A, S1B, S1C for the sample S1 and S2A, S2B, S2C for the sample S2. Each measurement has a size of 5.12×5.12 µm^2 with a sampling interval of 5 nm. Figure 5 illustrates the AFM measurements of S1A and S2A.

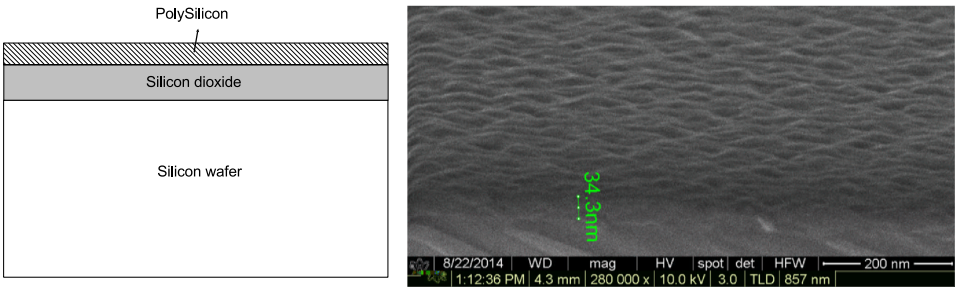

(a) Fabrication process (b) SEM of sample S1

Figure 4: Manufacturing of the poly-silicon surfaces. (a) Manufacturing steps. (b) SEM image of the sample S1.

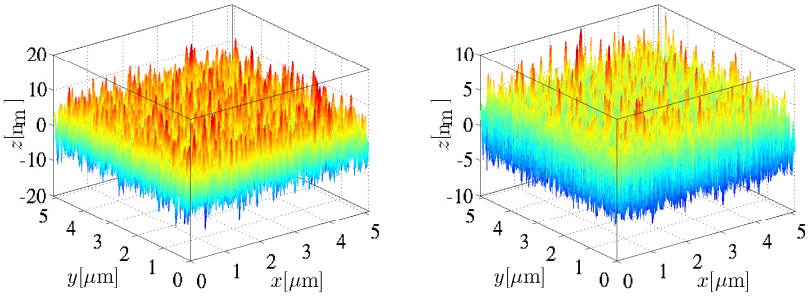

(a) S1A (b) S1B

Figure 5: AFM measurements of S1A and S2A samples. Note the different scale along the z-axis.

Table 2 collects the measurement statistical parameters including the roughness $\sqrt{m_0}$, with m_0 the variance of height, the variance of the height first derivatives m_2, and the variance of the height second derivatives m_4. To evaluate the derivatives from the 1024×1024 discrete data of each measurement, the topology is interpolated using cubic splines and the derivatives are calculated from this interpolation. The variances of the samples S1 and S2 are calculated as the means of their measurements variances.

3.2. Review on the asperity-based statistical rough surface contact theories

Considering the contact problem between a rough surface and a plane, the physical contact occurs at the highest asperities, as illustrated in Fig. 6(a). To evaluate the contact forces, the asperity-based rough surface contact theories use an important assumption: the interaction between the contacting asperities can be neglected. This assumption is verified when the real contact area is much smaller than the apparent area. Using this assumption the contact force per unit area between a rough surface S and a plane can be evaluated by

$$F^S(d) = \frac{1}{A(S)} \sum_{i=1}^{N^a} F^{a_i}(d), \tag{12}$$

where d is the distance between the mean plane of the rough surface to the flat surface, see Fig. 6(a), $A(S)$ is the apparent surface area, $F^{a_i}(d)$ is the contact force at asperity a_i, and N^a is the number of asperities on the considered surface. By assuming that an asperity can be approximated by a mathematically well-defined geometry such as a sphere, the force $F^{a_i}(d)$ can be evaluated by the asperity analytical contact models described in Section 2.2.

In the case of adhesive contact, the apparent adhesive energy, defined by the energy per unit area to

Table 2: The statistical parameters of the experimental surface topologies

	$\sqrt{m_0}$ [nm]	m_2 [−]	m_4 [nm^{-2}]
S1A	3.74	0.031	2.98×10^{-4}
S1B	4.00	0.040	5.09×10^{-4}
S1C	4.13	0.051	6.93×10^{-4}
S1	3.96	0.041	5.0×10^{-4}
S2A	2.04	0.021	4.92×10^{-4}
S2B	2.06	0.021	2.38×10^{-4}
S2C	2.13	0.026	4.81×10^{-4}
S2	2.08	0.023	4.04×10^{-4}

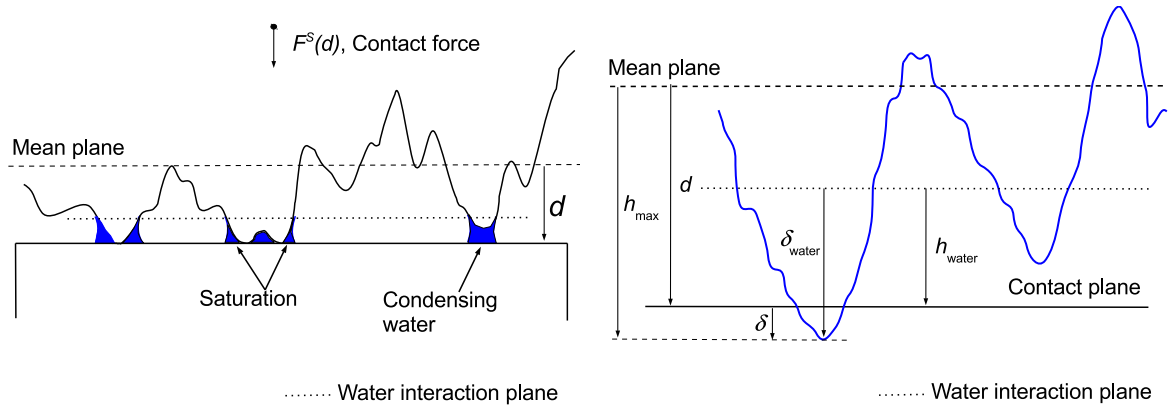

(a) Stiction between two surfaces

(b) Geometrical configuration

Figure 6: The stiction phenomenon. (a) Contact between a rough surface and a flat surface. The contact occurs at the highest asperities. (b) Configuration of the humid adhesive contact problem.

separate the two surfaces out of contact, is representative of the problem and can be calculated by

$$\Gamma^S = -\int_{-\infty}^{+\infty} F^S(d) 1_{\Re^-}(F^S(d)) \mathrm{d}d, \tag{13}$$

where $1_{\Re^-}()$ is equal to one if the argument is negative and zero otherwise.

The evaluation of Eq. (12) is not a trivial task. To simplify the problem, a statistical approach, such as in the works of Nayak [13] or Greenwood and Williamson [14] is commonly applied. In this approach, asperities are represented by their local maxima, which have zero first derivatives and negative second derivatives. This assumption leads to an approximation of the asperity radius from the geometrical mean curvature. The statistical approach assumes the surface height $z(x, y)$ to be a stationary Gaussian random field $\{Z(x, y), (x, y) \in T\}$, where T is a subset of $\Re^2$. From this assumption, Greenwood [15] has obtained the joint distribution $\rho^{\text{maxima}}(h, \kappa)$ of maxima curvature κ and height h as a function of the statistical parameters m_0, m_2, and m_4. Assuming each maximum represents one asperity, based on the joint distribution of maxima height and maxima curvature, the contact forces (12) are rewritten

$$F^S(d) = N \int_{-\infty}^{+\infty} \int_{\kappa_{\min}}^{\kappa_{\max}} F^a(h, \kappa, d) \rho^{\text{maxima}}(h, \kappa) \mathrm{d}\kappa \mathrm{d}h, \tag{14}$$

where $F^a(h, \kappa, d)$ is the asperity contact force evaluated using the asperity contact theory, and $N = \frac{1}{6\pi\sqrt{3}} \left(\frac{m_4}{m_2}\right)$ is the number of maxima per unit area [13].

This statistical approach has four limitations when applied to the humid stiction problem, among which the first two have been pointed out by Greenwood himself [19]:

(i) there is a confusion between an asperity and a maximum which are assumed to be the same; in fact an asperity can contain many maxima;

(ii) the asperity radius approximated by the local curvature can suffer from an important underestimation;

(iii) this method neglects the interaction of menisci at high humidity, also called the saturation phenomenon [1], in which the menisci of different asperities merge together, see Fig. 6(a);

(iv) as an average solution (infinite surface), this approach does not take the surface size into account, nor the topology uncertainties for a finite surface size.

Because of these disadvantages, the computed results usually differ from the experimental results. E.g. in [1] the original GW statistical approach predicted almost no stiction at low humidity contrarily to the experimental results. To close this gap, instead of using the infinite limits of the asperity height in the integration of the contact forces, Eq. (14), lower cutoff values were used. Although this cutoff can be justified in case of plasticity, for poly-silicon the obtained GW plasticity parameter is $\Psi = 0.8$ which makes the plasticity neglectable. This parameter proposed by GW [14] reads

$$\Psi = \frac{E}{2\,(1-\nu^2)\,H}\sqrt{\frac{\sigma_s}{R}}, \tag{15}$$

where H is the hardness and σ_s the yield stress and characterize the importance of plasticity. When $\Psi < 0.6$ the deformation remains elastic, when $\Psi > 1$ the deformation is predominantly plastic, and for a value of $\Psi = 0.8$ the plasticity can be neglected.

In the next section we propose a method based on the modified DMT approach to overcome these drawbacks.

3.3. Modified DMT approach for the rough surface adhesive contact problem

As discussed previously in Section 2.2, the modified DMT approach is more flexible in humid environments when applied on rough contacting bodies in comparison with the other asperity contact theory candidates, *i.e.* the Maugis and DMT models, as it is able to discriminate the contacting and adhesive scales.

As a reminder, in the modified DMT approach we assume that:

(i) the deformation due to the adhesive pressure inside the condensing water is negligible in comparison with the one resulting from the repulsive force;

(ii) at the water interaction plane, located at the distance h_{water} from the flat surface, see Fig. 6(b), the deformation of the asperity remains negligible.

These two assumptions of the modified DMT model were validated on a poly-silicon spherical asperity by comparing the prediction with the ones of Maugis theory in Section 2.2. Because of the first assumption, the contact force can be evaluated by the superposition of the repulsive Hertz contact force and of the capillary adhesive forces, which are computed separately as in the original DMT theory. The second assumption is used to evaluate the adhesive contact forces from the meniscus interface evaluated without accounting for the asperity profile deformation.

3.3.1. Adhesive contact forces of rough surfaces

Let us define the original surface profile by $z(x, y)$ and the height of the deformed surface profile by $z_{\text{def}}(x, y)$. For the configuration illustrated in Fig. 6(b), the adhesive contact force per unit apparent surface area can be evaluated, for an interference distance d, from

$$F^S(d) = \frac{1}{A(S)} \left[\sum_{i=1}^{N^a} F_r^{a_i}(d) + \Delta P \left(A\{\Omega^S_{\text{def}}(d - h_{\text{water}})\} - \sum_{i=1}^{N^a} A\{\Omega^{a_i}_{\text{def}}(d)\} \right) \right] \tag{16}$$

where

- $F_r^{a_i}$ is the repulsive force of asperity a_i;
- $\{\Omega^S_{\text{def}}(d - h_{\text{water}}) = \{(x, y)\} \subset \Re^2 : \quad z_{\text{def}}(x, y) \geq d - h_{\text{water}}\}$ is the footprint of the deformed surface profile on the water interaction plane, see Fig. 7(c);
- $A\{\Omega^S_{\text{def}}(d - h_{\text{water}})\}$ is area of $\Omega^S_{\text{def}}(d - h_{\text{water}})$;
- $\{\Omega^{a_i}_{\text{def}}(d) = \{(x, y)\} \subset \Re^2 : \quad z_{\text{def}}(x, y) \geq d\}$ is the contacting part of the deformed asperity a_i on the contact plane; and
- $A\{\Omega^{a_i}_{\text{def}}(d)\}$ is the area of $\Omega^{a_i}_{\text{def}}(d)$.

Using the second assumption, the area of the deformed surface footprint on the water interaction plane $A\{\Omega^S_{\text{def}}(d - h_{\text{water}})\}$ can be approximated by the area computed from the non deformed profile $A\{\Omega^S(d - h_{\text{water}})\}$ with $\{\Omega^S(d - h_{\text{water}}) = \{(x, y)\} \subset \Re^2 : \quad z(x, y) \geq d - h_{\text{water}}\}$ and can thus be directly estimated from the surface topology. The surface topology can be obtained either from AFM measurements, such as for the samples S1 and S2 presented in Section 3.4, or from numerically generated surfaces as discussed in Section 4. Because the area of the deformed surface footprint on the water interaction plane is calculated at the global surface scale (*i.e.* not asperity by asperity), the saturation phenomenon [1], in which the menisci of different asperities are merged, is treated automatically. The only two unknowns, the asperity repulsive force $F_r^{a_i}(d)$ and the asperity deformed contacting area $A\{\Omega^{a_i}_{\text{def}}(d)\}$, can be evaluated from Hertz solution.

However to apply the Hertz solution, the contacting asperities need to be approximated by spheres in the repulsive zone. This approximation is discussed in the next paragraph.

3.3.2. Asperity representation for evaluating the Hertz contact

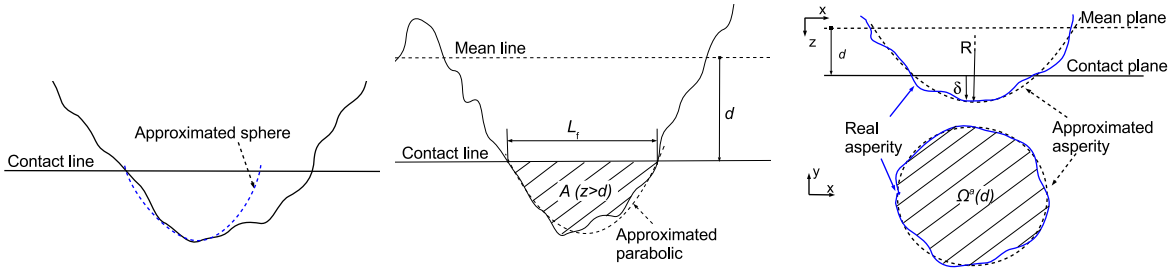

(a) Local maximum approximation (b) 2D approximation (c) 3D approximation

Figure 7: The approximation methods to evaluate the asperity radius. (a) The spherical radius approximated by the local maximum curvature suffers from an underestimation. (b) The 2D asperity is approximated by a parabolic curve. (c) The 3D asperity is approximated by a sphere.

The approximated radius obtained from the local maximum curvature can be an underestimation as it is based on local rules only, as illustrated in Fig. 7(a). Moreover, when computing m_4, the second derivatives of the surface profile are involved. However, when using surface topology measurements, these derivatives

depend on the sampling distance [30, 31]. These limitations inherent to local properties have motivated the development of a methodology based on more global measurements. To this end, Greenwood [19] figured out that the asperity curvature should take the contact interference into account, see Fig. 7(b). For 2D problems, the effective parabolic curvature of an asperity can be approximated by

$$\kappa = 12A(z > d)/L_f^3, \tag{17}$$

where $A(z > d)$ is the area of the asperity above the contact line at the distance d, and L_f is the length of its footprint on the contact line, see Fig. 7(b). In 3D, this method is not rigorous [19], as the effective curvatures have to be measured in several different directions. To overcome this limitation, we propose to define a sphere representing the asperity through an approximation process.

In this work, the asperity is approximated by a sphere whose parameters are the solutions of a least mean square error problem:

$$\begin{aligned}\min_{X^{a_i}=(x_0,y_0,z_0,R):X^{a_i}\in\Omega^{a_i}(d)\times\Re\times\Re^+} & E^{a_i}(X^{a_i},d) \\ = & \left[\frac{1}{A\{\Omega^{a_i}(d)\}}\int_{\Omega^{a_i}(d)}\left[z^{a_i}(x,y)-\left(\sqrt{R^2-(x-x_0)^2-(y-y_0)^2}+z_0\right)\right]^2\mathrm{d}\Omega\right]^{1/2},\end{aligned} \tag{18}$$

where the function E^{a_i} is the root mean square of the differences between the approximated sphere profile and the real asperity profile, $z^{a_i}(x,y)$ is the height function of the real asperity, (x_0, y_0, z_0) is the coordinate of the approximated sphere center, R is the radius of this sphere, $\{\Omega^{a_i}(d) = \{(x,y)\} \subset \Re^2 : \quad z(x,y) \geq d\}$ is the footprint of the asperity on the horizontal contact plane, see Fig. 7(c), and $A(\Omega^{a_i}(d))$ is the area of $\Omega^{a_i}(d)$. In 3D, the footprint $\Omega^{a_i}(d)$ can be numerically identified by using a flooding algorithm.

Solving the minimization problem of Eq. (18) to obtain the global solution is not trivial as the least mean square error function $E^{a_i}(X^{a_i}, d)$ is not strictly convex. To overcome the local minima of the error function, instead of solving the full problem of Eq. (18), we add an additional constraint which is the equality of the asperity footprint area $A\{\Omega^{a_i}(d)\}$ and of the approximated sphere footprint area $A\{\Omega^{s_i}(d)\}$ on the contact plane

$$A\{\Omega^{a_i}(d)\} = A\{\Omega^{s_i}(d)\} = \pi\left(R^2-(d-z_0)^2\right). \tag{19}$$

This additional constraint is also based on the fact that the repulsive force is proportional to the contacting area in the case of rough surfaces [14, 32]. Although, the value of the error function can be higher with this additional constraint, the numerical computation cost is reduced significantly as the z_0 coordinate of the sphere center can be directly obtained by

$$z_0 = d - \sqrt{R^2 - \frac{A\{\Omega^{a_i}(d)\}}{\pi}}. \tag{20}$$

The minimization of the least square error function thus becomes

$$\begin{aligned}\min_{X^{a_i}=(x_0,y_0,R):X^{a_i}\in\Omega^{a_i}(d)\times\Re\times\Re^+} & E^{a_i}(X^{a_i},d) \\ = & \left[\frac{1}{A\{\Omega^{a_i}(d)\}}\int_{\Omega^{a_i}(d)}\left[z^{a_i}(x,y)-\left(\sqrt{R^2-(x-x_0)^2-(y-y_0)^2}+\right.\right.\right. \\ & \left.\left.\left. d-\sqrt{R^2-\frac{A\{\Omega^{a_i}(d)\}}{\pi}}\right)\right]^2\mathrm{d}\Omega\right]^{1/2}.\end{aligned} \tag{21}$$

The unknowns $X^{a_i} = (x_0, y_0, R)$ can be determined using a Newton Raphson algorithm

$$X^{a_i(k+1)} = X^{a_i(k)} - \alpha^{(k)}\nabla E^{a_i}\left(X^{a_i(k)}\right), \tag{22}$$

where ∇E^{a_i} is the gradient vector of the least mean square error function E^{a_i}, $\alpha^{(k)}$ is the descent step vector which can be obtained from a line search algorithm, and where k is the actual iteration step. To quantify the error resulting from this asperity representation, we compare the global mean square error function E^S

$$E^S(d) = \sqrt{\frac{\sum_{i=1}^{N^a}[E^{a_i}(X^{a_i}, d)]^2 A\{\Omega^{a_i}(d)\}}{\sum_{i=1}^{N^a} A\{\Omega^{a_i}(d)\}}} \tag{23}$$

of the approximation process with the interference of the highest asperity, $\delta_{\max} = h_{\max} - d$ and with the silicon crystal unit-cell size. If the error remains smaller or comparable to the crystal unit-cell size the approximation is fully justified as the geometrical approximation is of the same order of the material structure. The Hertz theory can thus be applied on each asperity to evaluate its contribution to the repulsive forces $F_r^{a_i}$ and its contacting radius a^{a_i}.

3.4. Numerical results

In this section, the modified DMT approach is applied on the experimental measurements of the samples S1 and S2. The considered problem is the pull-out test between a rough surface and a flat surface. At first, the error of the asperity approximation represented by Eq. (23) is investigated. Secondly, the predictions obtained with the modified DMT approach are compared to the ones obtained with GW statistical approach. Finally we discuss the observed uncertainties on the obtained results.

3.4.1. Error on the asperity approximation

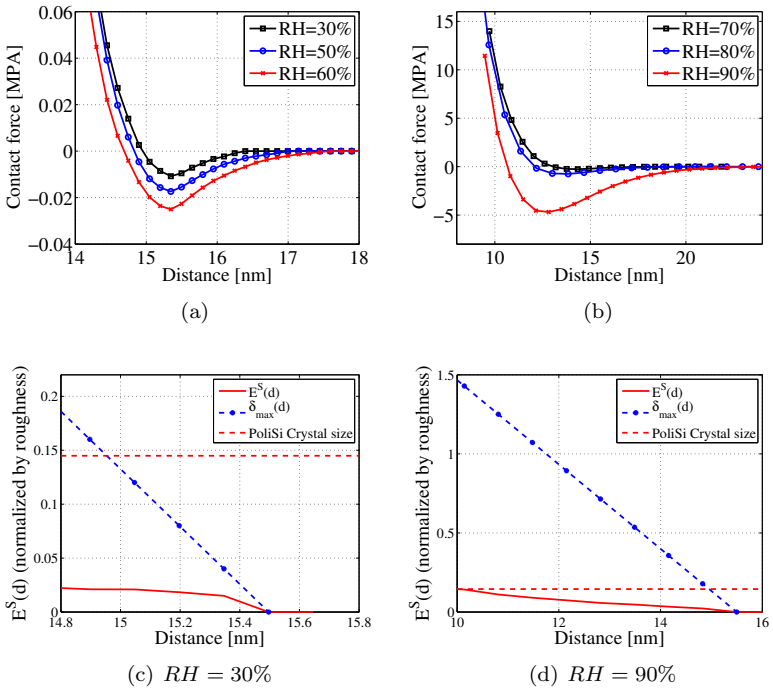

Figure 8: The numerical results obtained with the modified DMT method applied on the sample SA1: (a) the contact forces at RH={30%, 50%, 60%}, (b) the contact forces at RH={70%, 80%, 90%}, (c) the comparison of the approximation error $E^S(d)$ (23) with the interference of the highest asperity $\delta_{\max}$ and with the silicon crystal unit-cell size for RH = 30%, (d) the comparison of the approximation error $E^S(d)$ (23) with the interference of the highest asperity $\delta_{\max}$ and with the silicon crystal unit-cell size for RH = 90%.

The numerical results obtained with the modified DMT method for the sample S1A are given in Fig. 8. At high humidity levels, the adhesive forces are more important and the equilibrium distances, at which the

contact force is zero, are closer to the flat surface. For distances at which the contact forces are negative, which are of interest when studying the stiction case, the approximation errors E^s obtained by Eq. (23) remain much smaller than the interference $\delta_{\max}$ and always below the size of the silicon crystal unit-cell size, see Figs. 8(c) and 8(d).

3.4.2. Comparison of the statistical approach with the modified DMT approach.

The modified DMT approach is compared with the statistical approach developed by GW and expressed by Eq. (14). For the GW approach, for which the surface is assumed to have an infinite size, the topology is characterized by unique values, m_0, m_2, and m_4. With the new approach, the surface size is finite and the samples measurements are different. Thus we will obtain different predictions for the different topology measurements S1A, S1B, S1C of the same sample S1, as they correspond to different locations. Moreover, with the GW approach, the integral limits of Eq. (14) have effects on the results. After a convergence analysis, for the curvature κ integral limits, we select $[\kappa_{\min}, \kappa_{\max}] = [0.1\sqrt{m_4}, 2.5\sqrt{m_4}]$ corresponding to $R_{\max} = 447$ nm and $R_{\min} = 19$ nm, respectively. Several cutoff distances are also investigated for the integral limits on the asperity height.

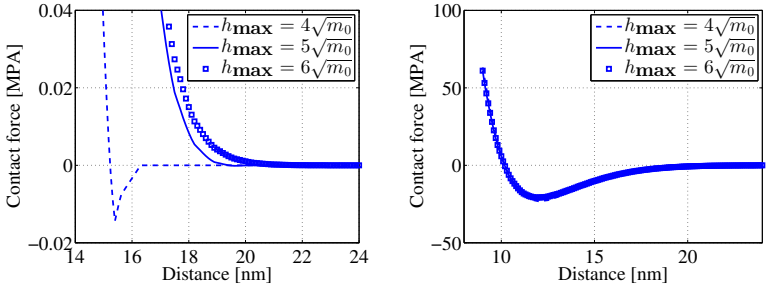

(a) $RH = 30\%$ (b) $RH = 90\%$

Figure 9: The convergence analysis of the integral limit $h_{\max}$ in the GW method.

The effect of cutoff in the asperity height is illustrated in Fig. 9 for the two extreme humidity levels. At 30% humidity level, the solutions have converged for $h_{\max} = 6\sqrt{m_0}$. However with this value there is almost no stiction predicted contrarily to what has been observed in [1]. In [1] it was shown that a cutoff distance of $2.5\sqrt{m_0}$ allows the GW approach to recover the experimental values.

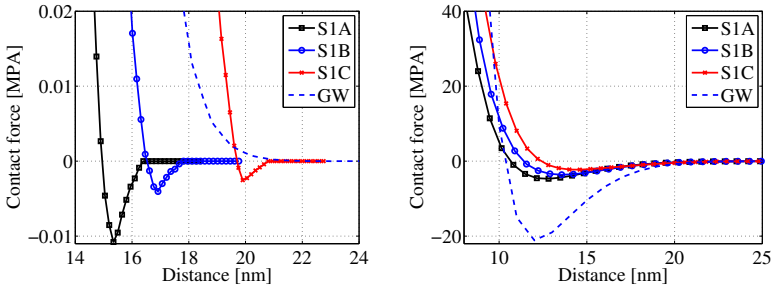

(a) $RH = 30\%$ (b) $RH = 90\%$

Figure 10: The numerical results obtained with the modified DMT approach and GW method for sample S1. The modified DMT approach is applied for the measurements at different locations, *i.e.* S1A, S1B, and S1C, and the GW method is applied using the statistical parameters of the sample S1.

The results obtained with the modified DMT approach applied on the measurements S1A, S1B, and S1C, and with the GW method applied on sample S1, are illustrated in Fig. 10. GW results are not reliable

due to the four drawbacks mentioned in Section 3.2. In particular, at low humidity the converged GW solution predicts almost no stiction while for high humidity the stiction is overestimated. At low humidity, the modified DMT predictions exhibit an important uncertainty in the contact forces and in the equilibrium distances. As the GW method results in an average solution, this method cannot capture these uncertainties. At high humidity, when the uncertainties are less important, the GW method leads to closer results to the modified DMT approach solutions. However, as mentioned in Section 3.2, the GW statistical approach cannot account for the saturation effect, consequently, its predictions are overestimated. For instance, at $RH = 90\%$ its maximum predicted negative contact forces, $F_{\max} = 20$ MPa, is higher than the Laplace pressure, $\Delta P = 14$ MPa. This fact is due to the presence of the saturation phenomenon, which is neglected with the GW method but which is naturally accounted for in the new approach.

3.4.3. The observed uncertainties in the apparent adhesive energy

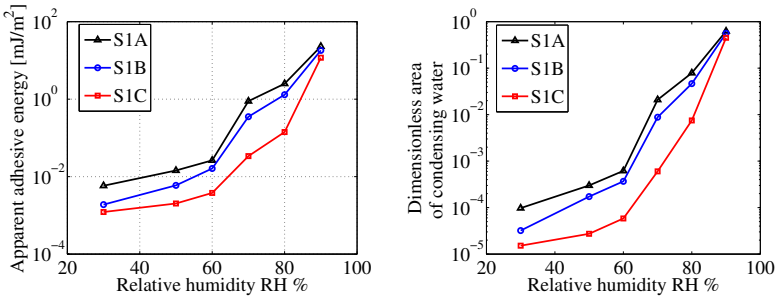

(a) Apparent adhesive energy (b) Condensing water area

Figure 11: (a)Apparent adhesive energies for the different experimental topology measurements from the sample S1. (b) The dimensionless area of condensing water at equilibrium position for the different experimental topology measurements of sample S1.

As mentioned previously, Fig. 10 illustrates that the contact forces evaluated at different locations, S1A, S1B, and S1C, of sample S1 are different although they are evaluated from the same experimental sample. The apparent adhesive energies computed from Eq. (13) for the different samples are reported in Fig. 11(a). This apparent energies are the representative values of the humid stiction problem and they also exhibit an important uncertainty. These uncertainties are larger at low humidity levels and decrease at higher humidity levels. They reflect the contact nature of the rough surfaces for which the contacting area is very small in comparison with the apparent area, especially at low humidity levels. Indeed, the dimensionless areas of condensing water $\frac{\left(A\{\Omega^S_{\text{def}}(d-h_{\text{water}})\}-\sum_{i=1}^{N^a} A\{\Omega^{a_i}_{\text{def}}(d)\}\right)}{A(S)}$ are shown in Fig. 11(b) where it can be seen that they are much smaller than one and have a large range of uncertainties for the low humidity levels. These uncertainties in the adhesive contact energies are reported in the literature: in [1] at 70% humidity the difference of the highest and lowest measured values of the apparent adhesive energy is about 200%; in [2] this difference is about 300% at 85% humidity. The importance of the uncertainties in the contact forces and in the apparent adhesive energies motivates the development of a stochastic analysis, as proposed in the next section.

4. Probabilistic rough surface adhesive contact model

In this section, we develop a probabilistic model based on the Monte Carlo method to predict the uncertainties related to the adhesive contact forces.

As it was shown in Section 3, the knowledge of the surface topology is an essential data to evaluate the contact forces. This topology can be measured from experimental samples, however, this is not practical to quantify the uncertainties illustrated in Fig. 11(a) as it would require a huge number of measurements. Instead of using directly the measurements, a numerical method is considered to generate the surface topology.

By considering surfaces as a second order stationary and Gaussian random field, the probabilistic model is built in three steps: (i) characterizing the surfaces by their psd function which can be obtained from a limited amount of surface measurements; (ii) generating different surfaces from this psd function; (iii) calculating the contact forces for each generated surface by applying the modified DMT approach presented in Section 3.3 in order to obtain the probabilistic distributions of the apparent adhesive energy.

4.1. Surface characterization

By assuming that the surface topology $z(x,y)$, the surface height at position (x,y), is a second order stationary and Gaussian random field as $\{Z(x,y),(x,y)\in\mathcal{T}\}$ with $\mathcal{T}\subset\Re^2$, the surfaces can be characterized by the covariance function c_Z from $\Re^4$ to $\Re$ defined by [33, 34]

$$c_Z\left((x,y),(\tilde{x},\tilde{y})\right)=E\left(Z(x,y)Z(\tilde{x},\tilde{y})\right)=\int_{\Re^2}z(x,y)\tilde{z}(\tilde{x},\tilde{y})\rho_{Z(x,y),\tilde{Z}(\tilde{x},\tilde{y})}(z,\tilde{z})\mathrm{d}z\mathrm{d}\tilde{z}, \tag{24}$$

where $E()$ is the estimation operation, and $\rho_{Z(x,y),\tilde{Z}(\tilde{x},\tilde{y})}$ is the second order marginal probability density function. Because the surfaces are considered as a stationary Gaussian random field, the covariance function is independent of (x,y), $c_Z((x,y),(\tilde{x},\tilde{y}))=c_Z(d_x=\tilde{x}-x,d_y=\tilde{y}-y)$. The two-dimensional random field can be alternatively characterized by a psd function from $\Re^2$ to $\Re$ and defined as the Fourier transform of the correlation function, *i.e.*

$$s_Z\left(\xi_x,\xi_y\right)=\int_{\Re^2}c_Z(d_x,d_y)\exp\left(-i(\xi_x d_x+\xi_y d_y)\right)\mathrm{d}d_x\mathrm{d}d_y. \tag{25}$$

The psd function is obtained by applying the Fourier transform (25) with the covariance function obtained from Eq. (24). In addition to this indirect method, the psd function can be estimated directly as follows

$$s_Z(\xi_x,\xi_y)=\lim_{\mathcal{X}\to\infty}\frac{1}{\mathcal{X}^2}|\hat{z}(\xi_x,\xi_y)|^2, \tag{26}$$

where $\mathcal{X}$ is the surface size, and $\hat{z}(\xi_x,\xi_y)$ is the Fourier transform of the surface topology $z(x,y)$ with a truncated size $\mathcal{X}\times\mathcal{X}$

$$\hat{z}(\xi_x,\xi_y)=\int_{-\infty}^{+\infty}\int_{-\infty}^{+\infty}1_{[-\mathcal{X}/2,\mathcal{X}/2]\times[-\mathcal{X}/2,\mathcal{X}/2]}(x,y)z(x,y)\exp\left(-i(\xi_x x+\xi_y y)\right)\mathrm{d}x\mathrm{d}y, \tag{27}$$

where $1_{[-\mathcal{X}/2,\mathcal{X}/2]\times[-\mathcal{X}/2,\mathcal{X}/2]}(x,y)$ is equal to 1 if $(x,y)\in[-\mathcal{X}/2,\mathcal{X}/2]\times[-\mathcal{X}/2,\mathcal{X}/2]$ and equal to zero otherwise. In practice the surface topology, obtained from the samples measurements, is a discrete function $z\left(x_{k_x},x_{k_y}\right)$ of $\mu\times\mu$ points in the space domain as $\left\{\left(x_{k_x},y_{k_y}\right),\quad 1\le k_x,k_y\le\mu\right\}$ with $\left\{\left(x_{k_x},y_{k_y}\right)=\left(-\mathcal{X}/2+\left(k_x-1\right)\Delta x,-\mathcal{X}/2+\left(k_y-1\right)\Delta x\right),\ 1\le k_x,k_y\le\mu\right\}$ and $\Delta x=\mathcal{X}/\mu$. The Fourier transform $\hat{z}(\xi_x,\xi_y)$ can be estimated using the Shannon/Poisson formula as

$$\begin{aligned}\hat{z}(\xi_x,\xi_y)=1_{[-\xi_L,\xi_L]\times[-\xi_L,\xi_L]}(\xi_x,\xi_y)(\Delta x)^2\\ \times\sum_{k_1=-\mu/2}^{\mu/2-1}\sum_{k_2=-\mu/2}^{\mu/2-1}z(x_{k_x=k_1+\mu/2+1},y_{k_y=k_2+\mu/2+1})\exp\left(-ik_1\Delta x\xi_x-ik_2\Delta x\xi_y\right)\end{aligned} \tag{28}$$

where $\xi_L=\pi/\Delta x$ is the highest frequency, and $1_{[-\xi_L,\xi_L]\times[-\xi_L,\xi_L]}(\xi_x,\xi_y)$ is equal to 1 if $(\xi_x,\xi_y)\in[-\xi_L,\xi_L]\times[-\xi_L,\xi_L]$ and equal to zero otherwise. By sampling the wave number domain as $\{(\xi_{l_x},\xi_{l_y}),\quad 1\le l_x,l_y\le\mu\}$ such that $\{(\xi_{l_x},\xi_{l_y})=(-\xi_L+(l_x-1)\Delta\xi,-\xi_L+(l_y-1)\Delta\xi),\ 1\le l_x,l_y\le\mu\}$, with $\Delta\xi=2\xi_L/\mu$, the Fourier transform $\hat{z}(\xi_{l_x},\xi_{l_y})$ (28) can be estimated by [33, 34]

$$\begin{aligned}\hat{z}(\xi_{l_x},\xi_{l_y})=(\Delta x)^2\Bigg[\sum_{k_1=-\mu/2}^{\mu/2-1}\sum_{k_2=-\mu/2}^{\mu/2-1}z(x_{k_x=k_1+\mu/2+1},y_{k_y=k_2+\mu/2+1})\exp\left(i\pi k_1+i\pi k_2\right)\\ \exp\left(-ik_1\frac{2\pi}{\mu}(l_x-1)-ik_2\frac{2\pi}{\mu}(l_y-1)\right)\Bigg],\end{aligned} \tag{29}$$

which can be rewritten as

$$\hat{z}(\xi_{l_x},\xi_{l_y}) = (\Delta x)^2 \exp\left(i(\mu/2+1)\frac{2\pi}{\mu}(l_x-1) + i(\mu/2+1)\frac{2\pi}{\mu}(l_y-1)\right) \times \sum_{k_x=1}^{\mu}\sum_{k_y=1}^{\mu} z(x_{k_x},y_{k_y}) \exp\left(i\pi(k_x-\mu/2-1)+i\pi(k_y-\mu/2-1)\right) \exp\left(-ik_x\frac{2\pi}{\mu}(l_x-1) - ik_y\frac{2\pi}{\mu}(l_y-1)\right). \tag{30}$$

This equation can be computed using the fast Fourier transform (FFT) to reduce the computational cost.

In fact the psd function calculated from Eq. (26) with the discrete Fourier transform obtained from Eq. (28) is an estimation. To reduce the variance in this estimation, the psd function can be estimated by averaging the calculated psd functions for different surface topologies measured at different locations of the same sample following the method reported in [33], *i.e.* by

$$s_Z = \frac{1}{n}\sum_{j=1}^{n} s_Z^{(j)}, \tag{31}$$

where n is number of surfaces, and $s_Z^{(j)}$ is the psd function of the surface j and obtained from Eq. (26).

Variance - bias analysis of the psd function. There are two conditions to be fulfilled when estimating the psd function, the convergence in Eq. (26), and the reduction of the variance using Eq. (31). In our case, there are 3 measurements available at three different locations for each sample S1 and S2. To reduce the variance, more samples are required. To this end, each measurement is divided into smaller sub-surfaces. However to make sure the sub-surfaces remain representative of the initial ones, we investigate the precision of the surface height variances by considering the following condition on the standard derivation of the surface height variances

$$\frac{\sqrt{E\left(\left[m_0^{(j)} - m_0\right]^2\right)}}{m_0} << 1, \tag{32}$$

where $m_0^{(j)}$ is the height variance of the surface j with $j \in \{1..n\}$, and m_0 is the global variance of the surface height taken from Tab. 2.

We investigate the psd functions obtained in three ways: (i) from 3 measurements of size $5.12 \times 5.12\,\mu m^2$ with $\mu = 1024$; (ii) from 12 sub-surfaces of size $2.56 \times 2.56\,\mu m^2$ with $\mu = 512$ (each measurement is divided into 4 sub-surfaces); (iii) from 48 sub-surfaces of size $1.28 \times 1.28\,\mu m^2$ with $\mu = 256$ (each measurement is divided by 16). In all the three cases, the sampling distance in the space domain is 5nm. The psd functions obtained with the three schemes applied on the sample S1 are illustrated in Figs. 12(a)-(c). For the three schemes, the standard derivations of the surface height variances, Eq. (32), are smaller than 3%: the sub-surfaces remains representative. Moreover as the psd function obtained with the three surfaces, which has the lowest bias, does not exhibit sharp changes in its general trend, see Fig. 12(a), the bias introduced by sub-divising each surface into 4 or 16 sub-surfaces remains low. In order to have the minimum variance when estimating the psd function, the third scheme is thus chosen. The psd function of sample S2 topology obtained using the third scheme is illustrated in Fig. 12(d).

As the calculated psd functions can contain high frequencies that do not reflect the real data, their frequencies are filtered, *i.e.* the maximum frequency ξ is set to $\xi_{\max}$, in order to have an equivalence between the spacial variances of the measurements (variance of height m_0, variance of first derivatives m_2, variance of second derivatives m_4) with the respective psd moments (zero order moment μ_0, second order moment μ_2, and fourth order moment μ_4), which are reported in Tab. 3.

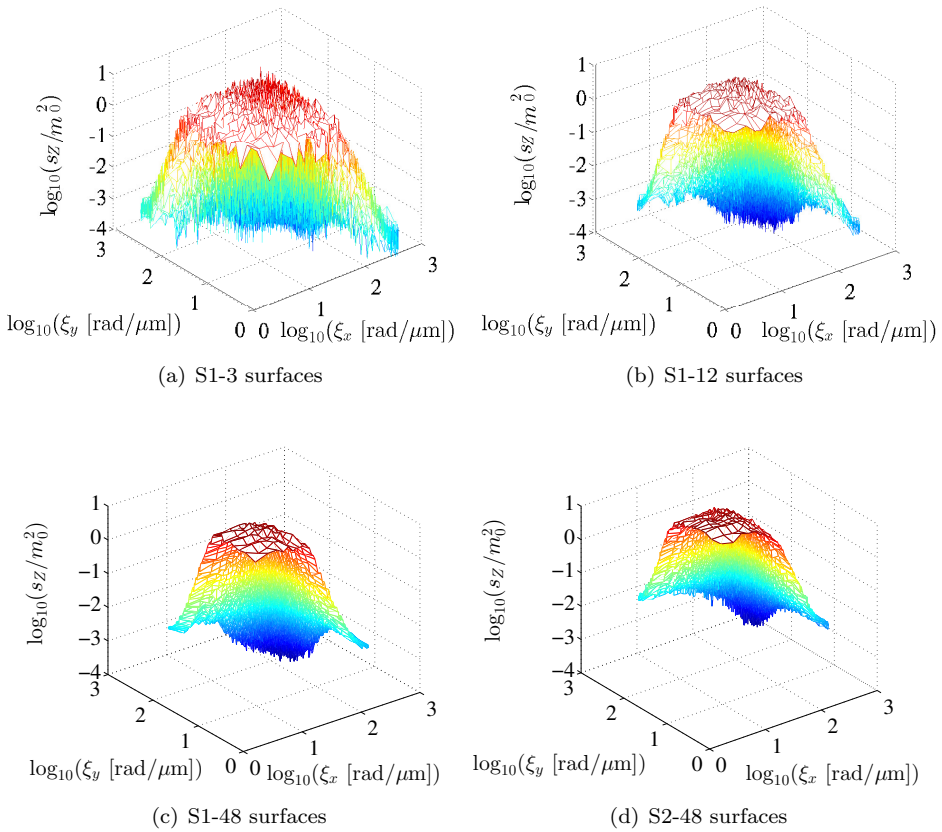

(a) S1-3 surfaces

(b) S1-12 surfaces

(c) S1-48 surfaces

(d) S2-48 surfaces

Figure 12: (a-c) The psd functions obtained from the sample S1 measurements with the three numerical schemes: (a) Scheme 1: 3 surfaces of size $5.12 \times 5.12\,\mu\text{m}^2$ with $\mu = 1024$, (b) scheme 2: 12 sub-surfaces of size $2.56 \times 2.56\,\mu\text{m}^2$ with $\mu = 512$, (c) scheme 3: 48 sub-surfaces of $1.28 \times 1.28\,\mu\text{m}^2$ with $\mu = 256$. (d) The psd function obtained from the sample S2 measurements with the third numerical scheme.

4.2. Surface generation

By assuming a stationary and Gaussian random field for a chosen value of the maximum wave number μ, surfaces can be generated following the works of Shinozuka [22] and Poiron and Soize [23], with

$$z^{(\mu)}(x,y) = \sqrt{2\Delta\xi^2}\,\text{Re}\left(\sum_{l_x=1}^{\mu}\sum_{l_y=1}^{\mu}\zeta_{(l_x,l_y)}\sqrt{\frac{1}{(2\pi)^2}s_Z(\xi_{l_x},\xi_{l_y})}\exp\left(ix\xi_{l_x}+iy\xi_{l_y}+i\phi_{(l_x,l_y)}\right)\right) \tag{33}$$

where

- $\{s_Z(\xi_{l_x},\xi_{l_y}),\quad (\xi_{l_x},\xi_{l_y}) \in \Re^2\}$ is the psd function;
- the values $\{(\xi_{l_x},\xi_{l_y}),\quad 1 \le l_x, l_y \le \mu\}$ are samplings of the wave number domain such that $\{(\xi_{l_x},\xi_{l_y}) = (-\xi_L + (l_x-1)\Delta\xi, -\xi_L + (l_y-1)\Delta\xi),\ 1 \le l_x, l_y \le \mu\}$, with $\Delta\xi = 2\xi_L/\mu$;
- the values $\{\phi_{(l_x,l_y)},\quad 1 \le l_x, l_y \le \mu\}$ are $\mu \times \mu$ independent realizations of a uniform random variable with values in $[0, 2\pi]$; and
- the values $\{\zeta_{(l_x,l_y)},\quad 1 \le l_x, l_y \le \mu\}$ are such that $\{\zeta_{(l_x,l_y)} = -\sqrt{-\log(\psi_{(l_x,l_y)})},\quad 1 \le l_x, l_y \le \mu\}$, where $\{\psi_{(l_x,l_y)},\quad 1 \le l_x, l_y \le \mu\}$ are $\mu \times \mu$ independent realizations of a uniform random variable with values in $[0, 1]$.

Table 3: Comparison of the spacial variances and psd moments of samples S1 and S2.

	μ_0 [nm^2]	μ_2 [-]	μ_4 [nm^{-2}]
Sample S1			
Spacial variances of measurements	15.7	0.041	5.00×10^{-4}
Psd moments with cutoff frequency $\xi_{\max} = 289$ rad $\cdot$ µm^{-1}	15.7	0.040	5.08×10^{-4}
Sample S2			
Spacial variances of measurements	4.30	0.023	4.04×10^{-4}
Psd moments with cutoff frequency $\xi_{\max} = 289$ rad $\cdot$ µm^{-1}	4.32	0.021	3.99×10^{-4}

The implementation of Eq. (33) is costly in terms of computational resources due to the double sum operation. To reduce the computational time, we rely on the inverse fast Fourier transform (iFFT) scheme. By sampling the $\mathcal{X}\times\mathcal{X}$ space domain into $\mu\times\mu$ points as $\{(x_{k_x}, y_{k_y}), \quad 1 \le k_x, k_y \le \mu\}$ with $\{(x_{k_x}, y_{k_y}) = (-\mathcal{X}/2 + (k_x - 1)\Delta x, -\mathcal{X}/2 + (k_y - 1)\Delta x) \quad 1 \le k_x, k_y \le \mu\}$ and $\Delta x = \chi/\mu$, the surface height at the sampling points is rewritten from Eq. (33) as

$$z^{(\mu)}(x_{k_x}, y_{k_y}) = \sqrt{2\Delta\xi^2}\,\mathrm{Re}\left(\sum_{l_x=1}^{\mu}\sum_{l_y=1}^{\mu}\zeta_{(l_x,l_y)}\sqrt{\frac{1}{(2\pi)^2}s_Z(\xi_{l_x},\xi_{l_y})}\exp\left(ix_{k_x}\xi_{l_x} + iy_{k_x}\xi_{l_y} + i\phi_{(l_x,l_y)}\right)\right). \quad (34)$$

By setting $\Delta x = \pi/\xi_L$, the space domain sampling corresponds to the wave number domain sampling. By choosing μ as an exponent of two and using the detailed expressions of (ξ_{l_x}, ξ_{l_y}), (x_{k_x}, y_{k_y}), Eq. (34) can be implemented by applying the iFFT algorithm. Using the Monte Carlo method to generate the uniform random variable $\phi_{(l_x,l_y)}$ with values in $[0, 2\pi]$, Eq. (34) generates a set of independent and identically distributed surfaces.

4.2.1. From the experimental data to the surface generation

Practically, the sizes of the generated surfaces and of the experimental topology input data are not the same. Therefore, the estimation of the psd function is first discussed in more details in terms of the numerical algorithm before presenting the numerical results investigation.

As discussed in Section 4.1, to obtain the psd function, the input topology data is the surfaces $z(x_{k_x^0}, y_{k_y^0})$ with the sampling distance $\Delta x = 5$ nm and the size $\mathcal{X}^0 = 1.28\,\mu$m. The sampling in the space domain of these surfaces is $\{(x_{k_x^0}, y_{k_y^0}), \quad 1 \le k_x^0, k_y^0 \le \mu^0\}$ with $\{(x_{k_x^0}, y_{k_y^0}) = (-\mathcal{X}^0/2 + (k_x^0 - 1)\Delta x, -\mathcal{X}^0/2 + (k_y^0 - 1)\Delta x), \quad 1 \le k_x, k_y \le \mu^0\}$, and $\mu^0 = 256$. The sampling of their psd function is $\{(\xi_{l_x^0}, \xi_{l_y^0}) = (-\xi_L + (l_x^0 - 1)\Delta\xi^0, -\xi_L + (l_y^0 - 1)\Delta\xi^0), 1 \le l_x^0, l_y^0 \le 256\}$, with $\Delta\xi^0 = 2\xi_L/256$ and $\xi_L = \pi/5\,\mathrm{nm}^{-1}$.

Let us now assume we want to generate a $5.12\times5.12\,\mu\mathrm{m}^2$ surface with a sampling distance of $5\,\mathrm{nm}^{-1}$. The sampling of the wave number domain requires a higher resolution as $\{(\xi_{l_x}, \xi_{l_y}) = (-\xi_L + (l_x - 1)\Delta\xi, -\xi_L + (l_y - 1)\Delta\xi), 1 \le l_x, l_y \le 1024\}$, with $\Delta\xi = 2\xi_L/1024$ $(=\Delta\xi^0/4)$. The Fourier transform $\hat{z}(\xi_{l_x^0+p}, \xi_{l_y^0+q})$ at the additional points, $\{(\xi_{l_x^0+p}, \xi_{l_y^0+q}) = (-\xi_L + (l_x^0 + p - 1)\Delta\xi^0, -\xi_L + (l_y^0 + q - 1)\Delta\xi^0)$ with $p, q \in$

$\{0, -1/4, -1/2, -3/4\}\}$ can be estimated either by the following equation

$$\hat{z}(\xi_{l_x^0+p}, \xi_{l_y^0+q}) = (\Delta x)^2 \exp\left(i(\mu^0/2+1)\frac{2\pi}{\mu^0}(l_x^0+p-1) + i(\mu^0/2+1)\frac{2\pi}{\mu^0}(l_y^0+q-1)\right) \times \left[\sum_{k_x^0=1}^{\mu^0}\sum_{k_y^0=1}^{\mu^0} z(x_{k_x^0}, y_{k_y^0}) \exp\left(i\pi(k_x^0 - \mu^0/2 - 1 - k_x^0\frac{2}{\mu^0}p) + i\pi(k_y^0 - \mu^0/2 - 1 - k_y^0\frac{2}{\mu^0}q)\right) \times \exp\left(-ik_x^0\frac{2\pi}{\mu^0}(l_x^0-1) - ik_y^0\frac{2\pi}{\mu^0}(l_y^0-1)\right)\right], \tag{35}$$

on which we can apply the FFT algorithm, or by a interpolation process. To keep it simple in this work we use the interpolation process.

4.3. Numerical results

This section discusses the numerical results of the probabilistic approach. The considered physical problem is the same pull-out test as in the previous section.

4.3.1. Surface set generation

From the experimental topology measurements of samples S1 and S2, their psd functions are estimated, from which a set of independent and identically distributed surfaces can be generated. The modified DMT approach developed in Section 2.2.4 is applied on each generated surface to compute its adhesive contact force. In this work, the two surface sizes $5.12 \times 5.12\,\mu m^2$ and $10.24 \times 10.24\,\mu m^2$ are considered with a sampling distance of 5 nm in the space domain.

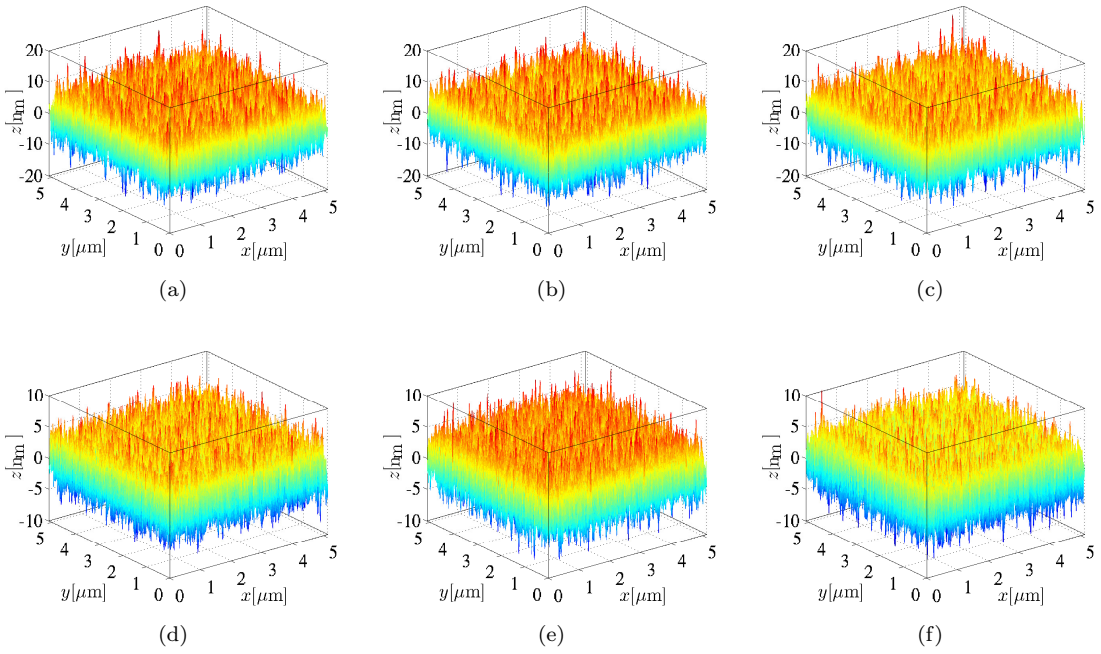

Figure 13: Examples of generated surfaces. (a-c) Three generated surfaces from the sample S1. (d-f) Three generated surfaces from sample S2. Note the difference of scales along the z-axis and the x- and y-axes.

The surface set can be generated from the psd function following the method described in Section 4.2. Some examples of generated surfaces are illustrated in Fig. 13.

4.3.2. Adhesive contact forces

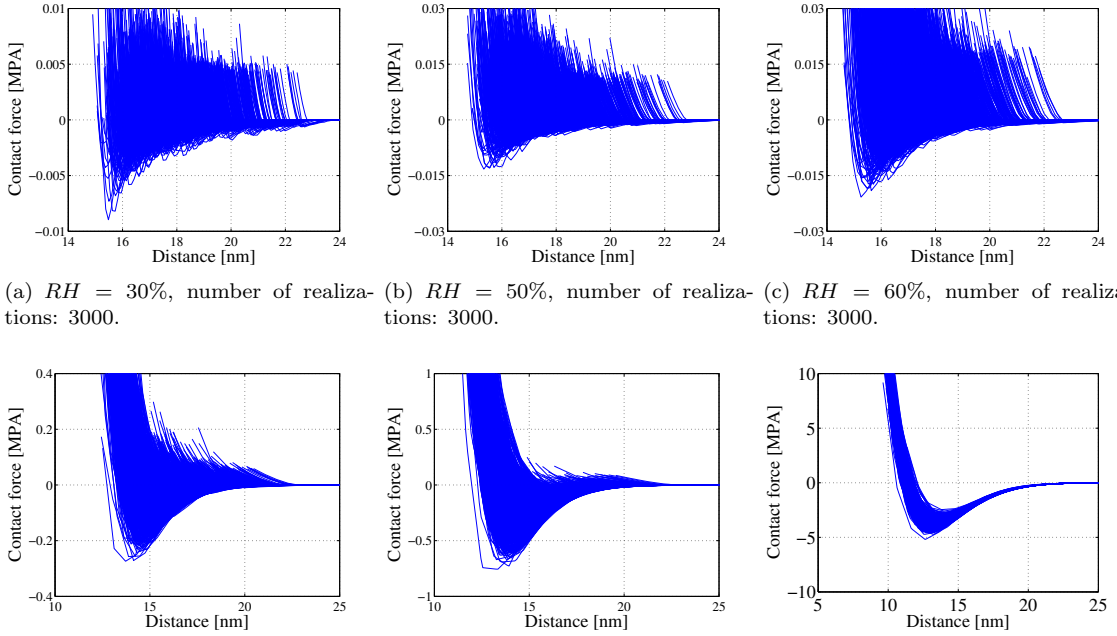

(a) RH = 30%, number of realizations: 3000. (b) RH = 50%, number of realizations: 3000. (c) RH = 60%, number of realizations: 3000.

(d) RH = 70%, number of realizations: 3000. (e) RH = 80%, number of realizations: 1500. (f) RH = 90%, number of realizations: 800.

Figure 14: The sets of adhesive contact forces at different humidity levels for the different generated surfaces of size $5 \times 5\,\mu m^2$ and having a psd function obtained from the sample S1 topology.

Figures 14 and 15 illustrate the adhesive contact curves obtained for each generated surface at different humidity levels, and for the psd functions obtained from the samples S1 and S2. The number of generated surfaces is such that a confidence range of 95% is reached. At the low humidity levels, the obtained results of the contact forces for the different generated surfaces show an important scattering. This uncertainty only decreases for the humidity levels higher than 80% in the sample S1 case, and higher than 70% in the sample S2 case. This scatter also exists when analyzing the apparent adhesive energies reported in Figs. 16(a) and 16(b).

On the one hand, at low humidity levels, $RH = \{30\%, 50\%, 60\%, 70\%\}$ for sample S1 and $RH = \{30\%, 50\%, 60\%\}$ for sample S2, due to the low heights of the condensing water, h_{water}, in comparison with the roughness of the surfaces, the area of the surface footprint on the condensing water plane $A(\Omega^S(d - h_{\text{water}}))$ is small. This results in small adhesive forces, small apparent adhesive energies, and a far equilibrium distances d_{eq} (for the sample S1 the observed equilibrium distance ranges, see Fig 14, are $[3.8\sqrt{m_0}, 5.7\sqrt{m_0}]$, $[3.6\sqrt{m_0}, 5.7\sqrt{m_0}]$, $[3.6\sqrt{m_0}, 5.7\sqrt{m_0}]$, $[3.3\sqrt{m_0}, 5.5\sqrt{m_0}]$ for the respective humidity levels $RH = \{30\%, 50\%, 60\%, 70\%\}$, while for the sample S2 the observed equilibrium distance ranges, see Fig. 15, are $[4\sqrt{m_0}, 6.2\sqrt{m_0}]$, $[3.5\sqrt{m_0}, 6.2\sqrt{m_0}]$, $[3.3\sqrt{m_0}, 5.5\sqrt{m_0}]$, for the humidity levels $RH = \{30\%, 50\%, 60\%\}$, respectively). Consequently, we observe a high scatter in the contact forces and in the apparent adhesive energies.

On the other hand, at the high humidity levels, $RH = \{80\%, 90\%\}$, the height of the condensing water, h_{water}, is high in comparison with the surface roughness, resulting in larger area of the surface footprint on the condensing water plane $A(\Omega^S(d - h_{\text{water}}))$. Consequently, the adhesive forces are larger, the apparent adhesive energies are higher, and the equilibrium distances d_{eq} are smaller (for the sample S1, the equilibrium distance ranges, see Fig. 14, are $d_{\text{eq}} = [3\sqrt{m_0}, 5.2\sqrt{m_0}]$ and $d_{\text{eq}} = [2.6\sqrt{m_0}, 3\sqrt{m_0}]$ for the humidity levels $RH = \{80\%, 90\%\}$, respectively, while for the sample S2 the equilibrium distance range, see Fig. 15, are $d_{\text{eq}} = [3\sqrt{m_0}, 5.2\sqrt{m_0}]$ and $d_{\text{eq}} = [2.6\sqrt{m_0}, 3\sqrt{m_0}]$ for the humidity levels $RH = \{80\%, 90\%\}$, respectively).

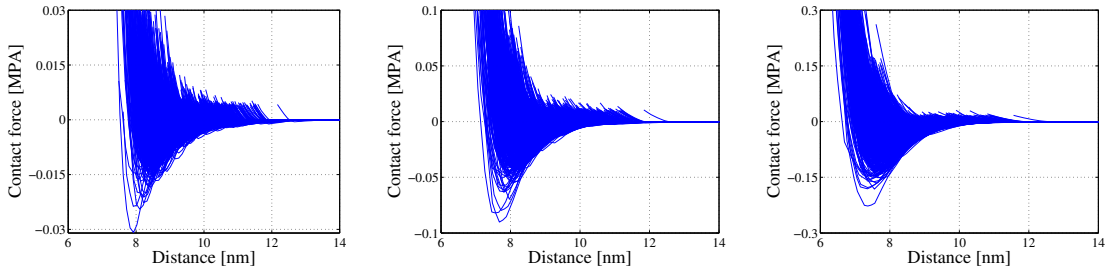

(a) $RH = 30\%$, number of realizations: 3000. (b) $RH = 50\%$, number of realizations: 2000. (c) $RH = 60\%$, number of realizations: 1500.

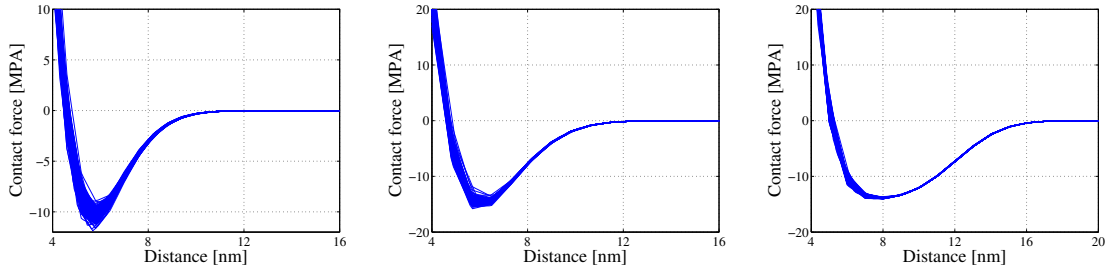

(d) $RH = 70\%$, number of realizations: 200. (e) $RH = 80\%$, number of realizations: 150. (f) $RH = 90\%$, number of realizations: 150.

Figure 15: The sets of adhesive contact forces at different humidity levels for the different generated surfaces of size $5 \times 5\,\mu m^2$ and having a psd function obtained from the sample S2 topology.

Thus, we observe less uncertainty at these two humidity levels. In particular, the contact forces at 80% and 90% humidity levels are almost constant for all the generated surfaces from the sample S2.

Figure 16(a) illustrates the effect of the surface size on the apparent adhesive energies. When increasing the size of the surfaces, there exists a higher probability for a higher asperity to interact, which increases the equilibrium distance and decreases the real surface contact. In turn, this reduces the apparent adhesive energy. This reduction is important at low humidity levels because the appearance of the higher asperities has a strong effect when the number of contacting asperities is small. In addition, by increasing the surface sizes, the uncertainties on the contact forces and on the apparent adhesive energies are less important as it can be observed at the high humidity levels. To illustrate this trend, the distribution functions of the apparent adhesive energies for the sample S1 are plotted in Fig. 17. At low humidity levels, when increasing the size of the surfaces, the obtained distributions move to the left due to the appearance of the higher asperities. For the high humidity levels, the variances of the distribution functions are smaller for the larger surface sizes and the average apparent adhesive energies for the different surface sizes are nearly coincident.

When comparing the samples S1 and S2, the sample S2 has the higher apparent adhesive energy due to its lower roughness. In addition, we observe in Fig. 15(f) a constant zone at the peak of adhesive contact forces. This is due to the saturation effect: when the menisci merge together and create a unique layer of water, the pressure inside this layer is equal to the Laplace pressure reported in Fig. 1(a).

5. Comparison with experiments

In this section, in order to evaluate the numerical model its predictions are compared with the experimental results of cantilever micro-beam adhesive tests reported in [2]. Instead of modeling the adhesive multiscale behaviors of cantilever beam structures –the multiscale aspect resuls from the non-constant rough surface mean planes distance along the beam length– which is beyond the scope of this paper, we consider the numerical results of the pull-out test described throughout this paper –for which the rough surface mean

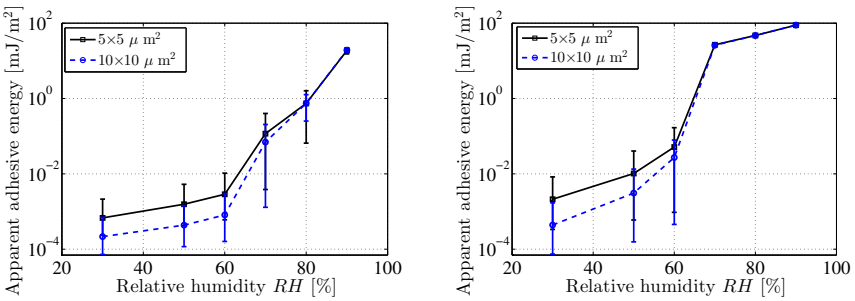

(a) S1 (b) S2

Figure 16: The distribution of the apparent adhesive energies. (a) Error bars of the apparent adhesive energies for a psd function obtained from the sample S1 with a 95% confidence range. (b) Error bars of the apparent adhesive energies for a psd function obtained from the sample S2 with a 95% confidence range.

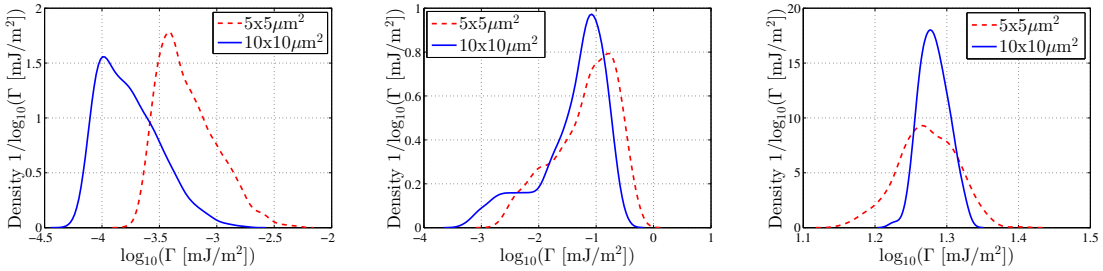

(a) $RH = 30\%$ (b) $RH = 70\%$ (c) $RH = 90\%$

Figure 17: The distribution of the apparent adhesive energies obtained from the set of generated surfaces having a psd function obtained from the sample S1 topology measurements.

planes distance remains constant along the surface. Moreover, as we do not have direct access to the surface topology, we build an equivalent psd function from the available data, which introduces an error in the model. Thus we will be careful when drawing the conclusions with respect to the experimental results as the nature of the tests is different. In a future work we intend to conduct experimental stiction tests on the measured samples S1 and S2 in order to validate more rigorously the model.

5.1. Description of the adhesive tests on cantilever beam structures

In [2], to investigate the adhesive behaviors, an array of cantilever beams interacting with their landing pads were fabricated using surfacial micro-machining processes. The cantilever beams have a width $w = 30\,\mu\text{m}$, a thickness $t = 2.62\,\mu\text{m}$, and a length l equal to $1500\,\mu\text{m}$. The gap from the cantilever beam lower side to the landing pad is $h = 1.9\,\mu\text{m}$, see Fig. 18(a). Both the landing pad and the cantilever beam are made of poly-silicon.

At the initial stage of the experiment, the cantilever beams were pulled into contact with the landing pad in dry environment by electrostatic forces. At the end of this stage, the cantilever beams can exhibit either an arc-shape or an s-shape, see Fig. 18(b). In the investigation stage, the humidity was increased by 5% humidity steps up to 95% humidity level. At each humidity level, the equilibrium shapes of the cantilever beams were recorded.

For an s-shape beam, the so-called crack length s defines the beginning of the contact equilibrium zone for which the contact force vanishes, see Fig. 18(b). The interaction zone $[s - \Delta s, s]$ is subjected to the adhesive forces between the beam lower surface and the landing pad surface, and is responsible for the

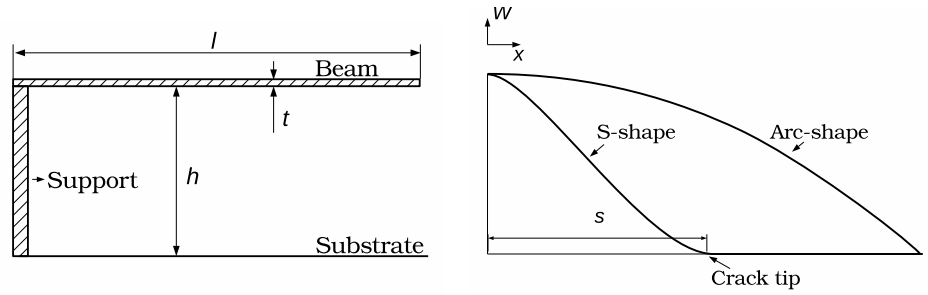

(a) Initial configuration (not on scale) (b) Contact equilibrium shapes

Figure 18: The cantilever beam structure: (a) initial configuration, (b) contacting equilibrium shapes.

stiction. The apparent adhesive energy can thus be evaluated from the equilibrium shapes [35] by

$$\Gamma = \frac{3}{2} E \frac{h^2 t^3}{s^4} \,. \tag{36}$$

This expression was used in [2] to extract the apparent adhesive energy from the described adhesive tests. However one should keep in mind that this analysis does not account for the randomness in the surface topology.

5.2. Description of numerical model

To apply our adhesive contact model, the adhesive contact of two rough surfaces $z_1(x, y)$ and $z_2(x, y)$ is treated as the contact between an equivalently surfaces $z(x, y) = z_1(x, y) + z_2(x, y)$ with a flat surface [36]. The developed adhesive contact model requires three inputs: the psd function of the equivalent surface topology, the size of the interacting area, and the evolution of the absorbed surface layer.

Table 4: The statistical surface parameters and the resulting psd function moments of the cantilever adhesive tests.

Experimental statistical parameters	Psd function moments
Roughness of the two surfaces [2]: $\sqrt{m_{01}}$=2.6 nm, $\sqrt{m_{02}}$ =2.4 nm	$\sqrt{\mu_0} = \sqrt{m_{01} + m_{02}}$=3.54 nm
Average asperity radius of the equivalent surface: $R = 220\,\text{nm}$	$\mu_4 = \dfrac{3\sqrt{\pi}}{8R} = 9.1\,\mu\text{m}^{-2}$
Number of asperities of the equivalent surface: N=80.1 µm^{-2}	$\mu_2 = \dfrac{1}{6\sqrt{3}\pi} \dfrac{\mu_4}{N} = 0.0035$

The first input, *i.e.* the psd function of the equivalent surface topology, is built using the roughness reported in [2]. To complete the data we assume that the average asperity radius of both surfaces is 440 nm, yielding an asperity radius of 220 nm for the equivalent surface, and a number of asperities of the equivalent surface of 80.1 µm^{-2}. Those estimations are close to the ones reported in [1] for another silicon surface obtained using a similar process. From these data, the moments of the psd function are estimated using the work of Nayak [13], and are reported in Tab. 4. In order to construct the psd function from the psd moments, we assume that:

- the surfaces are isotropic, consequently the psd function is symmetric such that $s_Z(\xi_r, \theta) = s_Z(\xi_r)$ with $\xi_r = \sqrt{\xi_x^2 + \xi_y^2}$ and $\theta = \tan^{-1} \frac{\xi_y}{\xi_x}$; and that

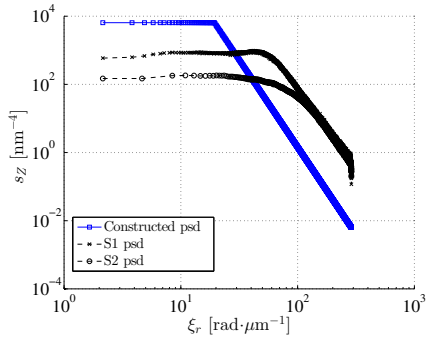

Figure 19: The approximated isotropic psd function of the experimental surfaces reported in [1]. The psd functions of surfaces S1 and S2 are given for references.

- the psd function has a self-affine shape, such that

$$s_z^{\text{const}}(\xi_r) = \begin{cases} s_Z^0 & \text{if } 0 \leq \xi_r < \xi_r^0 \ ; \\ s_Z^0 \left(\dfrac{\xi_r}{\xi_r^0} \right)^{\log_{10}\left(\frac{s_Z^1}{s_z^0}\right)/\log_{10}\left(\frac{\xi_{\max}}{\xi_r^0}\right)} & \text{if } \xi_r^0 \leq \xi_r \leq \xi_{\max} \ ; \\ 0 & \text{if } \xi_{\max} < \xi_r \ ; \end{cases} \tag{37}$$

  where s_Z^0, s_Z^1, ξ_r^0, and $\xi_{\max}$ have to be evaluated.

As we need to determine four parameters using three statistical moments, the maximum wave number $\xi_{\max}$ is chosen to be the same as with the one obtained for the samples S1 and S2 in Section 4.1, *i.e.* $\xi_{\max} = 289\ \text{rad} \cdot \mu\text{m}^{-1}$. The three remaining unknowns ξ_r^0, s_Z^0, and s_Z^1 are determined so that the moments μ_0, μ_2, and μ_4 of the psd function reported in Tab. 4, and μ_0^{const}, μ_2^{const}, and μ_4^{const} corresponding to the constructed psd function in Eq. (37) are equivalent. The resolution of this problem yields $\xi_r^0 = 19.4\ \text{rad} \cdot \mu\text{m}^{-1}$, $s_Z^0 = 6.46 \times 10^3\ \text{nm}^4$, and $s_Z^1 = 6.29 \times 10^{-3}\ \text{nm}^4$.The constructed psd function is illustrated in Fig. 19.

The second input, *i.e.* determining the sampling area of the interacting zone, cannot be directly obtained for the cantinlever beam experiments. Indeed, if for the pull-out tests the sampling area was corresponding to the experimental sample area, for the cantilever beam tests they correpsond to $\Delta s \times w$, as defined in Section 5.1, and result from the multiscale behavior of the adhesive contact. As first approximation we consider the interaction length Δs equal to the thickness of the beam with $\Delta s \times w = 2.62\,\mu\text{m} \times 30\,\mu\text{m}$.

Finally the third input, *i.e.* the evolution of the absorbed surface layer, is approximated using literature data. In the previous sections we have considered a layer containing three water molecules with a thickness of 0.9 nm for humidity levels above 65%, and we have neglected the absorbed surface layer below this humidity level following the argumentation in [2, 27]. We still consider this assumption, but for the sake of comparison we also consider the case without absorbed surface layers at any humidity levels.

5.3. Comparison between the numerical and experimental results

The apparent adhesive energies obtained using the numerical pull-out tests and extracted from the cantilever beam experiments using Eq. (36) are reported in Fig. 20.

In Fig. 20(a), the apparent adhesive energies of the pull-out numerical results, for which the absorbed surface layers are neglected, are compared to the experimental results reported in [2]. It can be seen that the numerical results predict a range of apparent adhesive energies overlapping the experimental measures except at 30% and 70% relative humidity levels. At 30% humidity the predicted energies are lower than for higher humidity levels contrarily to the experimental cases for which the measured energy remains constant at low humidity. However the difference remains small between the experiments and the numerical tests in regards with the assumptions as a change of 15% in the measured experimental crack length s results

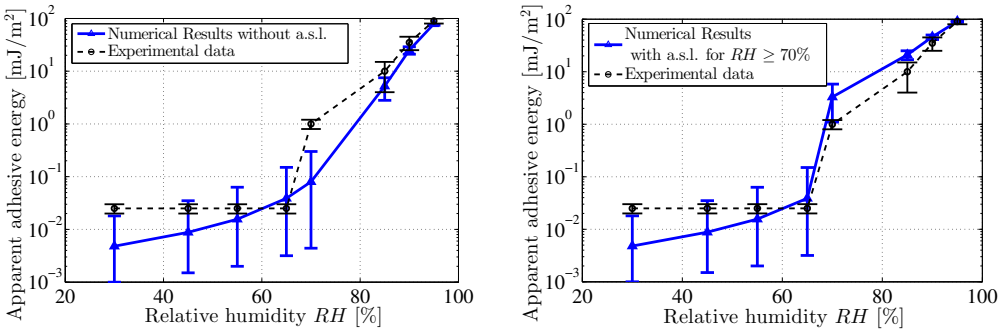

(a) Numerical results with no absorbed surface layer *vs.* the experimental results.

(b) Numerical results with absorbed surface layers above 65% humidity *vs.* the experimental results.

Figure 20: Comparison between the apparent adhesive energies of the pull-out numerical results and the cantilever beam adhesive tests. The confidence range of the numerical pull-out tests is 95%. (a) Comparison between numerical models, for which the absorbed surface layers are neglected, with the experimental results reported in [2]. (b) Comparison between numerical models, for which the absorbed surface layers above 65% humidity are considered, with the experimental results reported in [2].

in a change of 100% in the apparent adhesive energy, see Eq. (36). The difference at 70% humidity could be explained by the absorbed surface layers. When considering the absorbed surface layers above 65% relative humidity, it can be seen in Fig. 20(b) that the model recovers the same order of apparent adhesive energy as for the experiments at this humidity level, although the prediction at 85% are now slightly higher. As a generality the larger uncertainty range in the numerical tests than in the experimental data can be explained by the difference of the tests nature and is in agreement with the uncertainties in the surface topology. Indeed for the cantilever experimental tests, as the interacting length Δs is much smaller than the contacting length $l - s$, see Fig. 18(b), even if the adhesive contact forces in the zone $[s - \Delta s, s]$ are not high enough to induce stiction, it is possible that for a value of s' slightly higher than s the adhesive forces are high enough to lead to stiction. The apparent adhesive energy measured with the adhesive cantilever beam tests will thus exhibits a smaller uncertainty range.

The validation of the model requires further work. First experimental pull-out tests will have to be conducted to be able to directly validate the adhesive model. Then in order to predict the adhesive behavior of the cantilever beams, a stochastic multiscale model will have to be developed. In both cases, we will directly use the surface topology of the real samples to construct the psd function as in Section 4 in order to improve the accuracy. Finally more work will be required to characterize with accuracy the absorbed surface layer.

6. Conclusions

In this work, we have developed a framework to evaluate the uncertainties in the adhesive contact forces and apparent adhesive energy between a rough surface and a plane in humid environments.

When considering the asperity interactions, a modified DMT approach was proposed for hard materials and long range adhesive forces. This modified DMT approach has the advantage of being able to consider two different length scales for the repulsive and adhesive forces evaluations.

The modified DMT approach was thus applied on a rough surface whose topology was obtained from experimental measurements. This approach avoids the drawbacks of the common statistical approaches for rough surfaces. In particular it accounts naturally for the merge of menisci at high humidity levels and it avoids the recourse to a cutoff when integrating the asperity probabilistic distribution.

We have proposed an uncertainty quantification method by generating numerically rough surfaces from a psd function determined from experimental topological measurements. The method captures uncertainties, which results from the small ratio of the condensing water area to the apparent interacting surfaces area.

Finally we have compared the numerical results of pull-out tests with cantilever beam adhesive experiments. Although the predictions were in the right magnitude order, it appears that a stochastic multiscale model is needed to apply the model to cantilever beams studies or to other structures. In the meantime, the framework will be validated by conducting pull-in experiments to avoid this complexity.

Acknowledgment

The research has been funded by the Walloon Region under the agreement no 1117477 (CT-INT 2011-11-14) in the context of the ERA-NET MNT framework and by the Romanian UEFISCDI Agency contract ERA-NET MNT no 7-063 (2012-2015).

The authors from IMT Bucharest want to thank Phys. Raluca Gavrila for AFM measurements.

References

[1] M. de Boer, Capillary adhesion between elastically hard rough surfaces, Experimental Mechanics 47 (2007) 171–183. doi:10.1007/s11340-006-0631-z.
URL http://dx.doi.org/10.1007/s11340-006-0631-z

[2] F. W. DelRio, M. L. Dunn, M. P. de Boer, Van der waals and capillary adhesion of polycrystalline silicon micromachined surfaces, in: B. Bhushan (Ed.), Scanning Probe Microscopy in Nanoscience and Nanotechnology 3, NanoScience and Technology, Springer Berlin Heidelberg, 2013, pp. 363–393. doi:10.1007/978-3-642-25414-7-14.
URL http://dx.doi.org/10.1007/978-3-642-25414-7-14

[3] H. Hertz, Ueber die berührung fester elastischer körper., Journal für die reine und angewandte Mathematik 92 (1882) 156–171.
URL http://eudml.org/doc/148490

[4] K. L. Johnson, K. Kendall, A. D. Roberts, Surface energy and the contact of elastic solids, Proceedings of the Royal Society of London. A. Mathematical and Physical Sciences 324 (1558) (1971) 301–313. doi:10.1098/rspa.1971.0141.
URL http://rspa.royalsocietypublishing.org/content/324/1558/301.abstract

[5] B. Derjaguin, V. Muller, Y. Toporov, Effect of contact deformations on the adhesion of particles, Journal of Colloid and Interface Science 53 (2) (1975) 314 – 326. doi:10.1016/0021-9797(75)90018-1.
URL http://www.sciencedirect.com/science/article/pii/0021979775900181

[6] D. Maugis, Adhesion of spheres: The jkr-dmt transition using a dugdale model, Journal of Colloid and Interface Science 150 (1) (1992) 243 – 269. doi:10.1016/0021-9797(92)90285-T.
URL http://www.sciencedirect.com/science/article/pii/002197979290285T

[7] D. Maugis, B. Gauthier-Manuel, Jkr-dmt transition in the presence of a liquid meniscus, Journal of Adhesion Science and Technology 8 (11) (1994) 1311–1322. arXiv:http://dx.doi.org/10.1163/156856194X00627, doi:10.1163/156856194X00627.
URL http://dx.doi.org/10.1163/156856194X00627

[8] P.-R. Cha, D. J. Srolovitz, T. Kyle Vanderlick, Molecular dynamics simulation of single asperity contact, Acta Materialia 52 (13) (2004) 3983 – 3996. doi:http://dx.doi.org/10.1016/j.actamat.2004.05.014.
URL http://www.sciencedirect.com/science/article/pii/S1359645404002769

[9] W. Sun, The dynamic effect on mechanical contacts between nanoparticles, Nanoscale 5 (2013) 12658–12669. doi:10.1039/C3NR04354A.
URL http://dx.doi.org/10.1039/C3NR04354A

[10] W. Sun, Q. Zeng, A. Yu, K. Kendall, Calculation of normal contact forces between silica nanospheres., Langmuir 29. doi:10.1021/la401087j.
URL http://dx.doi.org/10.1021/la401087j

[11] W. Sun, Y. Li, W. Xu, Y.-W. Mai, Interactions between crystalline nanospheres: comparisons between molecular dynamics simulations and continuum models, RSC Advances 4 (2014) 34500–34509. doi:10.1039/C4RA05480F.
URL http://dx.doi.org/10.1039/C4RA05480F

[12] S.-S. Cho, S. Park, Finite element modeling of adhesive contact using molecular potential, Tribology International 37 (9) (2004) 763 – 769. doi:http://dx.doi.org/10.1016/j.triboint.2004.04.007.
URL http://www.sciencedirect.com/science/article/pii/S0301679X04000878

[13] P. R. Nayak, Random process model of rough surfaces, Journal of Tribology 93 (3) (1971) 398–407. doi:10.1115/1.3451608.

[14] J. A. Greenwood, J. B. P. Williamson, Contact of nominally flat surfaces, Proceedings of the Royal Society of London. Series A. Mathematical and Physical Sciences 295 (1442) (1966) 300–319. doi:10.1098/rspa.1966.0242.

[15] J. Greenwood, A simplified elliptic model of rough surface contact, Wear 261 (2) (2006) 191 – 200. doi:http://dx.doi.org/10.1016/j.wear.2005.09.031.
URL http://www.sciencedirect.com/science/article/pii/S004316480500462X

[16] L. Wu, V. Rochus, L. Noels, J. C. Golinval, Influence of adhesive rough surface contact on microswitches, Journal of Applied Physics 106 (11) (2009) 113502. doi:10.1063/1.3260248.
URL http://link.aip.org/link/?JAP/106/113502/1

[17] L. Wu, L. Noels, V. Rochus, M. Pustan, J.-C. Golinval, A micro - macro approach to predict stiction due to surface contact in micro electro-mechanical systems, Journal of Microelectromechanical Systems 20 (4) (2011) 976 –990. doi:10.1109/JMEMS.2011.2153823.

[18] L. Wu, J.-C. Golinval, L. Noels, A micro-model for elasto-plastic adhesivecontact in micro-switches: Application to cyclic loading, Tribology International 57 (0) (2013) 137 – 146. doi:http://dx.doi.org/10.1016/j.triboint.2012.08.003.
URL http://www.sciencedirect.com/science/article/pii/S0301679X12002757

[19] J. Greenwood, J. Wu, Surface roughness and contact: An apology, Meccanica 36 (6) (2001) 617–630. doi:10.1023/A:1016340601964.
URL http://dx.doi.org/10.1023/A1016340601964

[20] R. Ardito, A. Corigliano, A. Frangi, Modelling of spontaneous adhesion phenomena in micro-electro-mechanical systems, European Journal of Mechanics - A/Solids 39 (0) (2013) 144 – 152. doi:http://dx.doi.org/10.1016/j.euromechsol.2012.11.008.
URL http://www.sciencedirect.com/science/article/pii/S0997753812001489

[21] R. Ardito, A. Corigliano, A. Frangi, F. Rizzini, Advanced models for the calculation of capillary attraction in axisymmetric configurations, European Journal of Mechanics - A/Solids 47 (0) (2014) 298 – 308. doi:http://dx.doi.org/10.1016/j.euromechsol.2014.05.002.
URL http://www.sciencedirect.com/science/article/pii/S0997753814000679

[22] M. Shinozuka, Simulation of multivariate and multidimensional random processes, The Journal of the Acoustical Society of America 49 (1B) (1971) 357–368. doi:http://dx.doi.org/10.1121/1.1912338.
URL http://scitation.aip.org/content/asa/journal/jasa/49/1B/10.1121/1.1912338

[23] F. Poirion, C. Soize, Numerical methods and mathematical aspects for simulation of homogeneous and non homogeneous gaussian vector fields, in: P. Kre, W. Wedig (Eds.), Probabilistic Methods in Applied Physics, Vol. 451 of Lecture Notes in Physics, Springer Berlin Heidelberg, 1995, pp. 17–53. doi:10.1007/3-540-60214-3-50.
URL http://dx.doi.org/10.1007/3-540-60214-3-50

[24] S. Cai, B. Bhushan, Meniscus and viscous forces during separation of hydrophilic and hydrophobic surfaces with liquid-mediated contacts, Materials Science and Engineering: R: Reports 61 (16) (2008) 78 – 106. doi:http://dx.doi.org/10.1016/j.mser.2007.03.003.
URL http://www.sciencedirect.com/science/article/pii/S0927796X08000296

[25] F. W. DelRio, M. L. D. Dunn, M. P. de Boer, Capillary adhesion model for contacting micromachined surfaces, Scripta Materialia 59 (9) (2008) 916 – 920, viewpoint set no. 44 The materials for MEMS. doi:http://dx.doi.org/10.1016/j.scriptamat.2008.02.037.
URL http://www.sciencedirect.com/science/article/pii/S1359646208001668

[26] X. Xue, A. A. Polycarpou, Meniscus model for noncontacting and contacting sphere-on-flat surfaces including elastic-plastic deformation, Journal of Applied Physics 103 (2) (2008) –. doi:10.1063/1.2830863.

[27] D. B. Asay, S. H. Kim, Evolution of the adsorbed water layer structure on silicon oxide at room temperature, The Journal of Physical Chemistry B 109 (35) (2005) 16760–16763. arXiv:http://pubs.acs.org/doi/pdf/10.1021/jp053042o, doi:10.1021/jp053042o.
URL http://pubs.acs.org/doi/abs/10.1021/jp053042o

[28] K.-S. Kim, R. McMeeking, K. Johnson, Adhesion, slip, cohesive zones and energy fluxes for elastic spheres in contact, Journal of the Mechanics and Physics of Solids 46 (2) (1998) 243 – 266. doi:http://dx.doi.org/10.1016/S0022-5096(97)00070-7.
URL http://www.sciencedirect.com/science/article/pii/S0022509697000707

[29] B. D. Jensen, M. de Boer, N. Masters, F. Bitsie, D. A. LaVan, Interferometry of actuated microcantilevers to determine material properties and test structure nonidealities in mems, Microelectromechanical Systems, Journal of 10 (3) (2001) 336–346. doi:10.1109/84.946779.

[30] A. Majumdar, C. Tien, Fractal characterization and simulation of rough surfaces, Wear 136 (2) (1990) 313 – 327. doi:http://dx.doi.org/10.1016/0043-1648(90)90154-3.
URL http://www.sciencedirect.com/science/article/pii/0043164890901543

[31] L. Kogut, R. L. Jackson, A comparison of contact modeling utilizing statistical and fractal approaches, Journal of tribology 128 (1) (2006) 213–217.

[32] J. F. Archard, Elastic deformation and the laws of friction, Proceedings of the Royal Society of London. Series A. Mathematical and Physical Sciences 243 (1233) (1957) 190–205. arXiv:http://rspa.royalsocietypublishing.org/content/243/1233/190.full.pdf+html, doi:10.1098/rspa.1957.0214.
URL http://rspa.royalsocietypublishing.org/content/243/1233/190.abstract

[33] D. E. Newland, An introduction to random vibrations, spectral & wavelet analysis, Courier Dover Publications, 2012.

[34] C. Soize, Méthodes mathématiques en analyse du signal, Masson, Paris, 1993.

[35] C. Mastrangelo, C. Hsu, A simple experimental technique for the measurement of the work of adhesion of microstructures, in: Solid-State Sensor and Actuator Workshop, 1992. 5th Technical Digest., IEEE, 1992, pp. 208–212. doi:10.1109/SOLSEN.1992.228291.

[36] K. L. Johnson, K. L. Johnson, Contact mechanics, Cambridge university press, 1987.